The chromatin remodeller CHD4 regulates transcription factor binding to both prevent activation of silent enhancers and maintain active regulatory elements

Andria Koulle[1,2,4], Oluwaseun Ogundele[1,2], Devina Shah[1,2,5], India-May Baker[1], Maya Lopez[1], Nicola Reynolds[1,3], Ramy Ragheb[1,3], Ernest Laue[1,2] and Brian Hendrich[1,2,3]

1. Cambridge Stem Cell Institute, Jeffrey Cheah Biomedical Centre, University of Cambridge, Cambridge CB2 0AW, UK
2. Department of Biochemistry, University of Cambridge, Cambridge CB2 1GA, UK
3. Living Systems Institute, University of Exeter, Exeter EX4 4QD, UK

4. Current Address: Department of Life Sciences, Imperial College London, London, SW7 2AZ, UK
5. Current Address: University of Copenhagen, Novo Nordisk Foundation Center for Protein Research, Blegdamsvej 3B, 2200 Copenhagen, Denmark

All correspondence to Brian Hendrich: B.D.Hendrich@exeter.ac.uk

Abstract

Chromatin organisation and transcriptional regulation are tightly coordinated processes that are essential for maintaining cellular identity and function. ATP-dependent chromatin remodelling proteins play critical roles in control of genome structure and in regulating transcription across eukaryotes. Their essential nature, however, has made it difficult to define exactly how these functions are mediated. The chromatin remodeller CHD4 has been shown to be capable of sliding nucleosomes in vitro, and to regulate chromatin accessibility and gene expression in vivo. Using an inducible depletion system, here we identify a second mechanism of action for CHD4 in actively restricting the residence time of transcription factors on chromatin. Together these activities result in distinct, context-dependent outcomes: at highly accessible regulatory elements, CHD4 limits transcription factor binding to maintain regulatory function, while at low-accessibility euchromatic regions, it prevents transcription factor engagement and sustains chromatin compaction, thereby silencing cryptic enhancers. Collectively, these mechanisms enable CHD4 to reduce transcriptional noise while preserving the responsiveness of active regulatory networks.

Introduction

Cell state transitions are driven by the activity of transcription factors. Many transcription factors bind to specific DNA motifs within chromatin, but the frequency of these motifs within mammalian genomes far outnumbers sites at which protein binding is detectable. The ability of a transcription factor to recognise its cognate motif is influenced by how the DNA encoding that motif is packaged in chromatin. Accessible sites, i.e. those associated with a low density of intact nucleosomes, are more likely to be identified and bound by transcription factors than are inaccessible sites, i.e. those associated with higher nucleosome density. Controlling chromatin accessibility is therefore crucial for controlling transcription factor binding to cognate sites in regulatory regions. Transcription factor binding patterns will then determine which gene regulatory regions are used to drive gene expression and thereby define cell identity.

Vertebrate cells contain multiple proteins capable of using energy derived from ATP hydrolysis to remodel nucleosomes. These chromatin remodellers share a conserved sucrose non-fermentable 2 (SNF2) helicase-like ATPase domain but otherwise have various additional functional domains which impact how they organise chromatin, transcription and DNA repair (Hota and Bruneau, 2016; Narlikar et al., 2013). Chromatin remodellers play important roles

in mammalian development, and heterozygous mutations in the genes encoding them underlie a variety of developmental disorders in humans (Gourisankar et al., 2024; Hota and Bruneau, 2016; Pierson et al., 2019). Similarly, somatic mutations in chromatin remodeller subunit genes are increasingly being implicated in cancer initiation and/or progression (Lai and Wade, 2011; Martincorena et al., 2017; Wilson and Roberts, 2011).

CHD4 is an abundant ATP-dependent chromatin remodelling protein which plays important roles in chromatin organisation and cell fate decisions in many different aspects of metazoan development. Depletion of CHD4 in mouse or Drosophila cells, or overexpression of a dominant negative form of the protein, leads to increased chromatin accessibility at regulatory elements and DNase hypersensitive sites (Dieuleveult et al., 2016; Morris et al., 2014; Moshkin et al., 2012), indicating that it predominantly functions to compact chromatin. Its impact on gene expression is less clear-cut, however. One study found that while CHD4 acted to repress genes with bivalent promoters, its activity at active promoters (marked with H3K4Me3) mainly facilitated transcription in mouse embryonic stem cells (Dieuleveult et al., 2016). Another study found CHD4 controlled the probability of gene expression, rather than levels, during the first cell fate transition in mammalian embryogenesis (O'Shaughnessy-Kirwan et al., 2015). Several studies in somatic lineages have shown that CHD4 prevents lineage inappropriate gene expression during cell fate decisions in both mice and Drosophila (Arends et al., 2019; Aughey et al., 2023; Gómez-del Arco et al., 2016; Sreenivasan et al., 2021; Wilczewski et al., 2018; Yoshida et al., 2019). Exactly how CHD4 has this varied impact on chromatin and transcription has not been defined.

CHD4 is the predominant chromatin remodelling subunit of the Nucleosome Remodelling and Deacetylation (NuRD) complex (Wade et al., 1998; Xue et al., 1998; Zhang et al., 1998) . NuRD is a highly abundant chromatin remodeller present at active enhancers and promoters in many cell types. Its activity is important not only to regulate transcription but also the movement of enhancers in 3D space (Basu et al., 2023) , and to maintain genome integrity (Polo et al., 2010; Smeenk et al., 2010) . NuRD has been shown to exert two functions in mammalian cells: one is to control the nucleosome density at active enhancers, thereby regulating transcription factor binding, enhancer activity and transcriptional output (Bornelöv et al., 2018; Pundhir et al., 2023), while the other is to prevent low-level, inappropriate transcription across the genome (Burgold et al., 2019; Montibus et al., 2023; Ragheb et al., 2020; Saotome et al., 2024).

Although mouse ES cells can survive with a complete loss of the histone deacetylase subunit of NuRD (Burgold et al., 2019), loss of the chromatin remodelling component, CHD4, leads to cell death (Stevens et al., 2017). While we have used genetics to create NuRD-low or NuRD-null ES cells in the past to define NuRD function, in both cases, the remodelling subcomplex (CHD4, GATAD2A/B, CDK2AP1) remained on chromatin and the extent to which it could continue to remodel chromatin is not known (Bornelöv et al., 2018). As with any genetic change, it is also very difficult to know to what extent constitutive loss of protein activity has resulted in selection of cells using some compensatory mechanism to remain viable. CHD4 is also known to function outside of the NuRD complex (O'Shaughnessy-Kirwan et al., 2015; Ostapcuk et al., 2018; Williams et al., 2004) . Assessing the direct function of NuRD's remodelling activity is therefore difficult as knockout of the remodeller results in a non-viable cell, while knockdown or exogenous overexpression of a dominant negative version of the remodeller (Bornelöv et al., 2018; Feng and Zhang, 2001) will likely produce a heterogeneous mix of cells with varying levels of remodeller activity and displaying increasing degrees of cell cycle arrest and apoptosis over time.

The CHD4/NuRD function described at enhancers has been defined both in genetic mutants and over a time course of NuRD reintroduction to null cells (Bornelöv et al., 2018; Reynolds et al., 2012) . In contrast, the noise reduction function has been described in genetically NuRD-deficient or NuRD-null cells or after NuRD component knockdown (Burgold et al., 2019; Montibus et al., 2023; Ragheb et al., 2020; Saotome et al., 2024) , meaning that this could either be a primary function of NuRD or a downstream consequence and/or cell adaptation of NuRD deletion/depletion. For these reasons we have employed a degron system, which allows us to acutely deplete CHD4 protein in mouse ES cells and assess the consequences to chromatin and gene expression within minutes to hours of protein depletion, long before the cells begin to exhibit cell cycle defects.

Results

CHD4 has an immediate and widespread impact on chromatin accessibility

NuRD in mouse ES cells can exist in various forms and it can contain different paralogs of key components such as MBD2 or MBD3, GATAD2A or GATAD2B, HDAC1 or HDAC2, and MTA1, 2 and/or MTA3 (Reid et al., 2023). In embryonic stem cells NuRD has only one chromatin remodelling subunit: CHD4. We therefore created ES cell lines in which the endogenous *Chd4* alleles were homozygously tagged with a mini-Auxin inducible degron

99 (mAID) (Nishimura et al., 2009). CHD4-mAID was largely depleted from both the nucleoplasm
100 and chromatin within 60 minutes of Auxin addition (Fig. 1A). CHD4 depleted cells showed a
101 normal cell cycle profile until 24 hours of depletion, when they began to undergo cell cycle
102 arrest at the G1/S checkpoint (Fig. 1B). By 30 hours CHD4-depleted cells were undergoing
103 apoptosis, which increased through 48 hours. We therefore focused our analyses on the first
104 few hours after CHD4 depletion, well before cells started to undergo cell cycle arrest.
105 CHD4 depletion had an immediate and widespread impact on chromatin accessibility, as
106 measured by calibrated ATAC-seq. After 60 minutes of CHD4 depletion there were more than
107 thirteen thousand sites showing a significant change in accessibility, which increased to over
108 fifty thousand sites showing increased accessibility and eight thousand showing decreased
109 accessibility by 4 hours (Fig. 1C). These data are consistent with previous reports of overall
110 increased accessibility upon CHD4/dMi2 depletion by shRNA in mouse ES cells or Drosophila
111 S2 cells (Dieuleveult et al., 2016; Moshkin et al., 2012).
112 Differentially accessible regions increasing in accessibility upon CHD4 depletion exhibited
113 low accessibility and low overall enrichment for specific histone modifications associated
114 with active chromatin in undepleted cells (H3K27Ac, H3K4Me1, H3K4Me3), but not
115 H3K27Me3 (Fig. 1D,E). As a class, these sites predominantly mapped to inactive enhancers
116 and repetitive elements (Fig. 1F). They had very low average enrichment for CHD4 or MBD3
117 (Fig. 1G) and would likely not pass the threshold to be counted as “Peaks” in many ChIP-seq
118 or Cut&Run datasets. Low enrichment for active chromatin marks and NuRD components as
119 well as low but detectable accessibility indicates that these sites predominantly represent
120 silent and cryptic regulatory sequences. Upon CHD4 loss accessibility at these sites
121 increased two- to three-fold at 60 and 240 minutes of depletion (Fig. 1D) indicating that the
122 low level CHD4 enrichment at these sites may nevertheless be functionally relevant.
123 Sites showing decreased accessibility without CHD4 were highly accessible in undepleted
124 cells, enriched for marks of active chromatin such as H3K4Me1 and H3K27Ac, and to a lesser
125 extent H3K4Me3 (Fig. 1D,E), and often overlapped with known enhancers and promoters
126 (Fig.1F). These sites also showed high enrichment for CHD4 and MBD3 in the undepleted
127 state (Fig. 1G). Upon CHD4 depletion accessibility at these sites was reduced by less than
128 two-fold on average (Fig. 1D). We and others have previously shown that NuRD acts at active
129 enhancers (Basu et al., 2023; Bornelöv et al., 2018; Dieuleveult et al., 2016) and, consistent
130 with these findings, CHD4 depletion caused an average decrease in accessibility at active
131 enhancers (Fig. 1H). We therefore conclude that CHD4 activity maintains closed chromatin

generally at inactive regulatory sequences but also contributes to the maintenance of highly accessible chromatin at active sites.

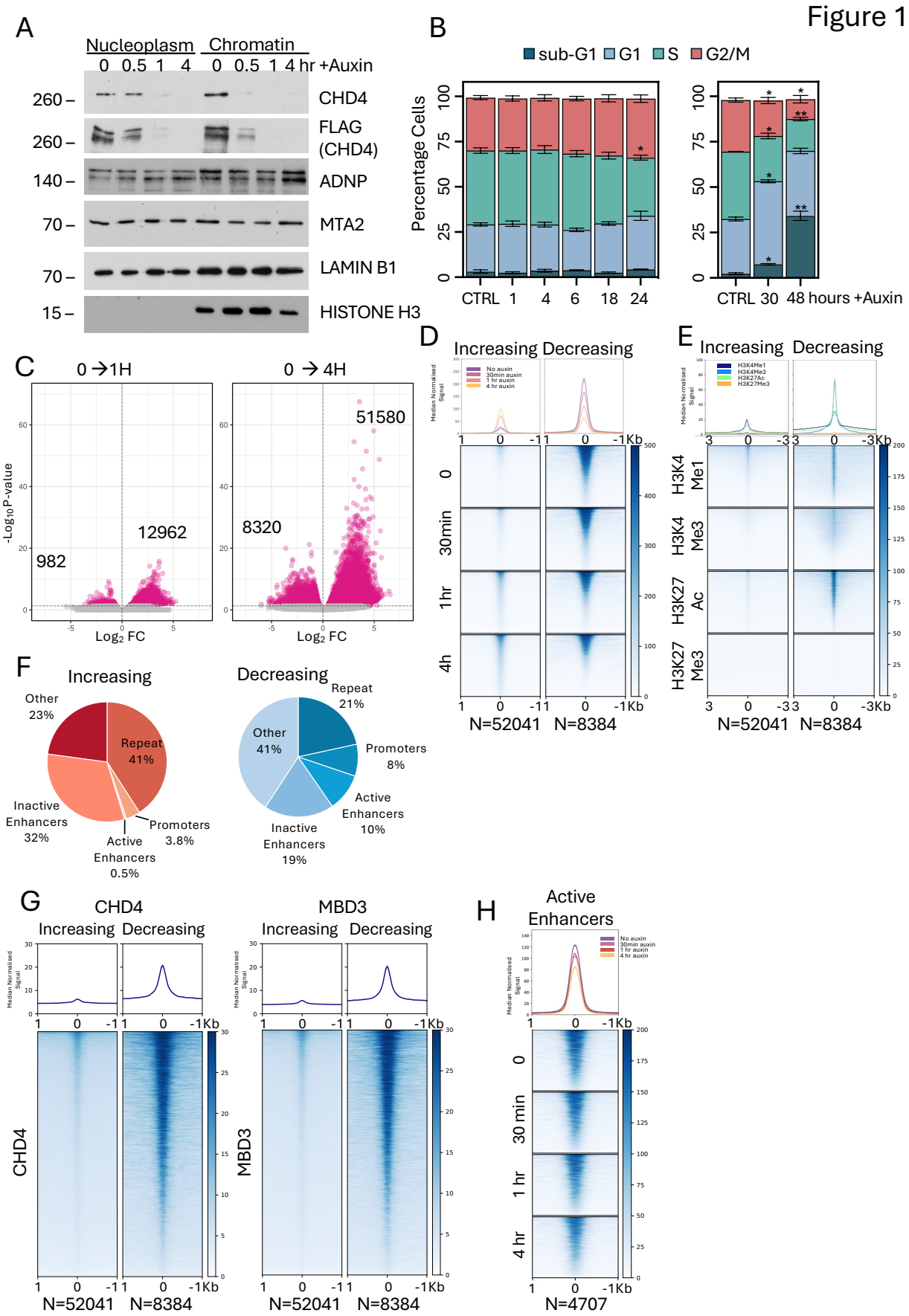

Figure 1. The impact of CHD4 depletion on chromatin accessibility. A. Western blots of nuclear soluble (Nucleoplasm) and chromatin fractions across CHD4 depletion probed with antibodies directed against indicated proteins. Times in hours of Auxin addition are indicated across the top. Lamin B1 and Histone H3 act as loading controls. **B**. Cell cycle analysis across CHD4 depletion time course. Hours post Auxin addition are indicated at the bottom, "CTRL" indicates DMSO control. Data represent an average of three replicates. Asterisks indicate significant differences from CTRL using a mixed-effects model with Dunnett's multiple comparisons correction. *$p < 0.05$; **$p < 0.01$. **C**. Volcano plots of differentially accessible ATAC-seq peaks between 0 and 1 hour of Auxin addition (left) or 0 and 4 hours of Auxin addition (right). Magenta spots indicate statistically significant differences (FDR > 0.05). Numbers of significant peaks decreased or increased are indicated on the plots. **D**. Heatmaps of ATAC-seq signal for all regions displaying increased accessibility (N=52041) or decreased accessibility (N=8384) at any time across the CHD4 depletion time course are displayed for each time point. **E**. Heatmaps of Cut&Run data for indicated histone modifications at sites increasing or decreasing in accessibility (as in panel **D**) (H3K27Ac and H3K4Me1 from this study; H3K27Me3 and H3K4Me3 taken from (Lando et al., 2024)) at indicated times after CHD4 depletion. **F**. Percentages of sites increasing in accessibility (top, blue) or decreasing in accessibility upon CHD4 depletion (bottom, red) which localise to indicated genomic features. Active enhancers are defined as having H3K4Me1 and K3K27Ac but not K3K4Me3, and inactive enhancers as having H3K4Me1 but not H3K4Me3 or H3K27Ac. **G**. Heatmaps of CHD4 and MBD3 Cut&Run data at upDARs and downDARs in 2iL conditions. **H**. Heatmaps of ATAC-seq signal at active enhancers (N=4707) across the CHD4 depletion time course. Median curves in graphs in **D**, **E**, **G** and **H** are plotted with standard error of the mean in lighter shading.

CHD4 activity maintains expression of active genes while reducing transcriptional noise

Significant changes in gene expression were first detected in nascent and total mRNA 1-2 hours after CHD4 depletion (Fig. 2A,B). Loss of CHD4 resulted in an approximately 2:1 ratio of increased to decreased gene expression from 1 hour onwards (Fig. 2C), consistent with CHD4 activity able to both facilitate and limit transcription, with most genes changing by two-fold or less (Fig. 2D). GO terms associated with activated genes indicate various tissue-specific functions, consistent with the general noise reduction activity described for NuRD (Burgold et al., 2019; Montibus et al., 2023; Ragheb et al., 2020). Downregulated genes, in contrast, are associated with cellular maintenance and early development, consistent with these genes being normally highly expressed in ES cells (Fig. 2E).

To assess whether the observed changes in chromatin accessibility were linked to changes in gene expression, we plotted the distance between differentially accessible regions and the annotated TSS of genes found to be misexpressed up to 4 hours after CHD4 depletion. Sites increasing in accessibility upon CHD4 depletion tended to be located far from genes repressed by CHD4 (Fig. 3A). This makes it unlikely that CHD4 directly silences gene expression by maintaining condensed chromatin at inactive promoters widely, although it

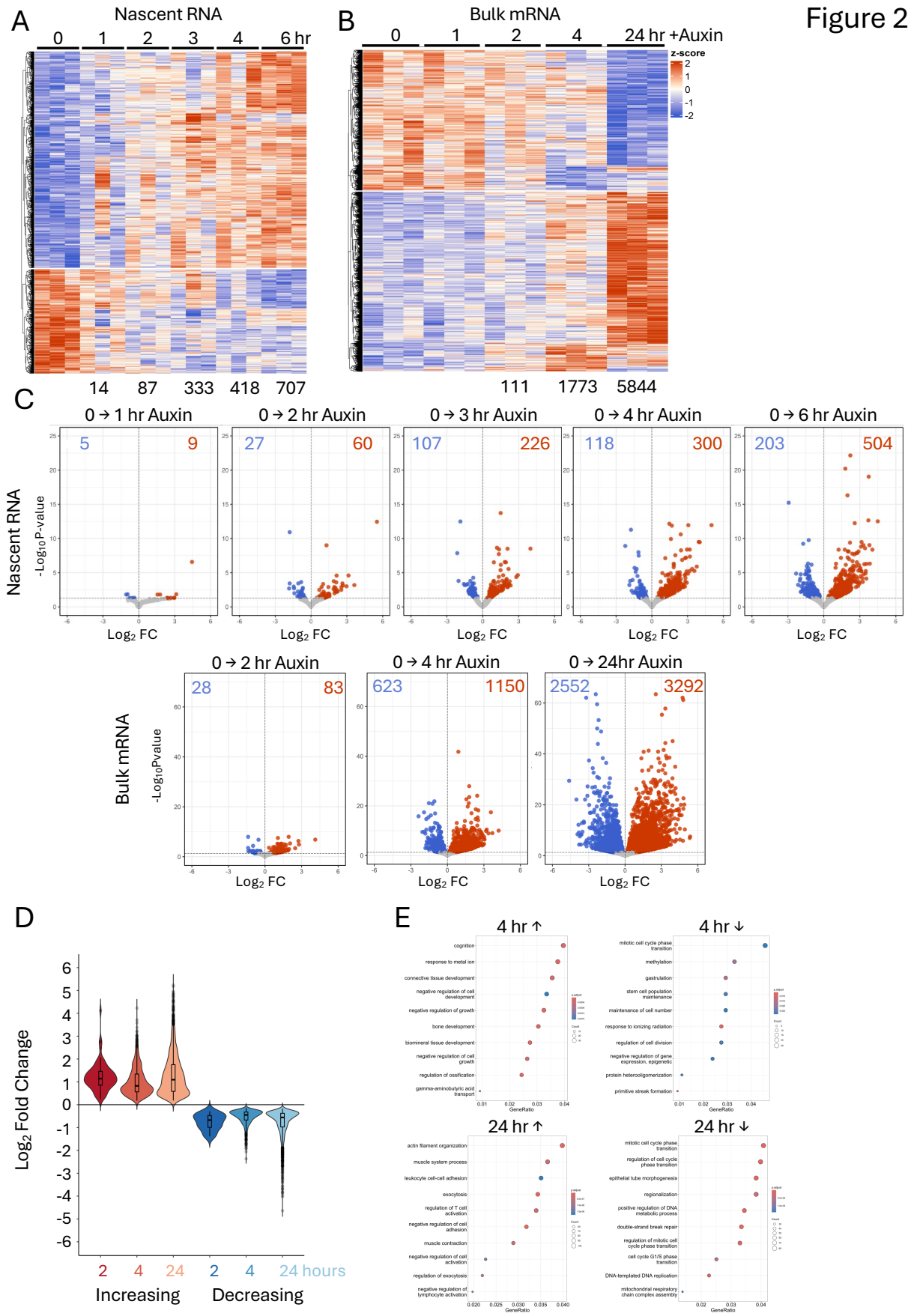

Figure 2. CHD4 acutely regulates gene expression. A and B. Heatmaps from nascent RNA-seq (A) or bulk RNA-seq (B) of genes showing significant (P_{adj} <0.05) changes in expression at any point during the CHD4 depletion time course. Heatmaps displays z-scores, meaning

expression for each gene has been centred and scaled across the entire time course. **C**. Volcano plots showing significant gene expression changes at indicated time points in nascent RNAseq (top) and bulk RNAseq (bottom). Genes increasing upon CHD4 depletion are shown in red, and those decreasing are shown in blue. The number of significantly misexpressed genes at each time point is indicated in the figure. **D**. Violin plots showing the average Log_2FoldChange of significant upregulated (red) and downregulated (blue) genes during the CHD4 depletion timecourse. **E**. Gene Ontology (GO) enrichment analysis of genes increased or decreased after four hours or 24 hours of CHD4 depletion. The top 10 biological processes are shown for each category, based on smallest adjusted p-value.

could be acting to prevent activation of distal enhancers. In contrast, a notable number of sites losing accessibility are located within 1Kb of the TSS of misregulated genes (Fig. 3A). This indicates that CHD4 acts at some highly active promoters to maintain both chromatin accessibility and transcriptional fidelity.

If loss of CHD4 resulted in activation of normally silent or cryptic enhancers, we would expect that they should show increases in enhancer-associated histone modifications and binding of transcription factors (TFs). As expected, Cut&Tag for H3K4Me1 and H3K27Ac showed increasing enrichment at CHD4-condensed sites 4 hours after CHD4 depletion, which did not increase further by 24 hours of depletion (Fig. 3B). Although these sites were largely unbound by NANOG or SOX2 in the presence of CHD4, within 1 hour of CHD4 depletion, they became extensively bound by both transcription factors (Fig. 3C). Consistently, thousands of new NANOG and SOX2 peaks were detected across the genome after CHD4 depletion (Fig. 3D). For example, the 25 kb region upstream of the *Eomes* gene contains multiple CHD4-condensed sites (Fig. 3E). Those labelled 1, 2 and 3 show very little, if any, accessibility or TF binding, and very low H3K27 acetylation and H3K4 monomethylation in undepleted cells. All three of these show a gain in accessibility, TF binding and both histone modifications upon CHD4 depletion. Those sites labelled 4 and 5 both show some accessibility, TF binding and enrichment for active histone modifications in undepleted cells. Nevertheless, these sites also show an increase in all of these features upon CHD4 depletion. In contrast, the nearby *Eomes* promoter ("P") shows little or no change in accessibility, TF binding or enrichment for H3K27Ac or H3K4Me1 across the CHD4 depletion time course.

We propose that low-level association of CHD4 and NuRD across euchromatin restricts chromatin accessibility, preventing transcription factors from binding to consensus sequence motifs. It is also possible, however, that accessibility increases are a consequence of more stable transcription factor binding. Failure to maintain this level of chromatin inaccessibility

results in activation of inactive and/or cryptic enhancers, which can stimulate inappropriate gene expression.

Figure 3

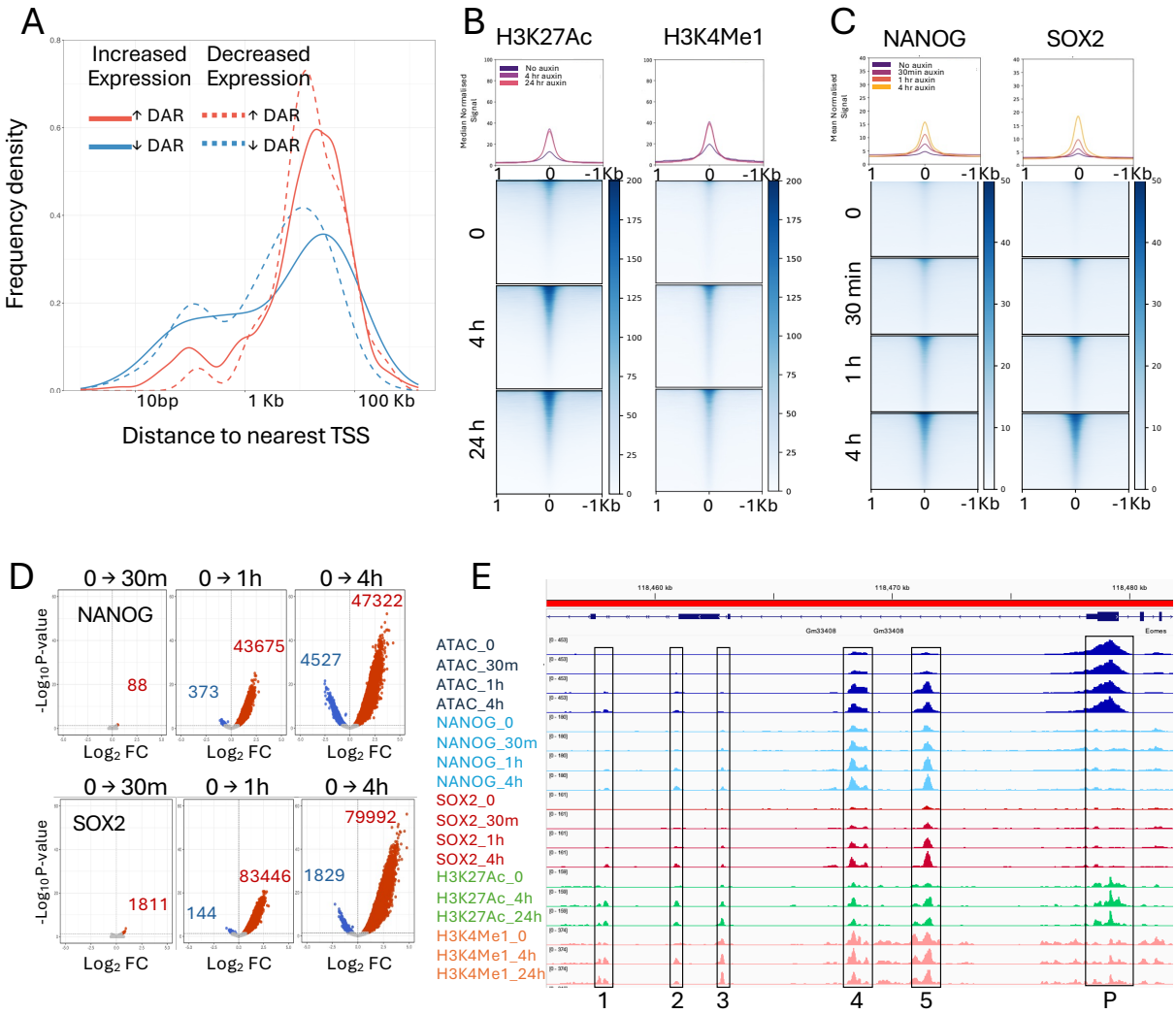

Figure 3. Chromatin opening upon CHD4 depletion. A. Frequency density distribution of the distance of increasing Differentially Accessible Regions ("↑ DARs," red lines) and decreasing regions ("↓ DAR," blue lines) to the TSS of genes showing increased (solid lines) or decreased (dotted lines) expression within four hours of CHD4 depletion. **B**. Heatmaps of Cut&Tag signal for H3K27Ac, and H3K4Me1 at sites increasing in accessibility (N = 52041) at indicated times of CHD4 depletion. **C**. Heatmaps of NANOG and SOX2 Cut&Run signal at increasing accessibility sites at indicated times of CHD4 depletion. Median curves in **B** and **C** are plotted with standard error of the mean in lighter shading. **D**. Pairwise comparisons of called peaks of binding for NANOG (top) and SOX2 (bottom) between undepleted cells (0h) and 30 minutes, 1 hour or 4 hours of CHD4 depletion. Significantly changed (FDR>0.05) binding sites are shown in blue when $\log_2$FC>0 and red when $\log_2$FC<0. **E**. IGV screenshot of the upstream region of the mouse *Eomes* locus displaying ATAC-seq, Cut&Run and Cut&Tag data as indicated at left. Boxed regions labelled 1-5 are CHD4 condensed sites, while the box labelled P corresponds to the *Eomes* promoter.

236 **CHD4 and SALL4 maintain chromatin inaccessibility largely independently**

237 The SALL4 protein is a very abundant transcription factor in mouse ES cells, which has long
238 been known to interact with the NuRD complex (Kloet et al., 2015; Lauberth and Rauchman,
239 2006; Lu et al., 2009; Miller et al., 2016). SALL4 preferentially binds to A/T-rich DNA genome-
240 wide, where it is proposed to exert a general repression function through NuRD recruitment
241 (Kong et al., 2021; Pantier et al., 2021; Ru et al., 2022; Watson et al., 2023). If this model is
242 correct, we would expect some proportion of the CHD4 condensed sites to be dependent
243 upon both CHD4 and SALL4 to remain inaccessible. To test this model, we assessed
244 chromatin accessibility after dTAG-mediated SALL4 depletion. SALL4 is partially redundant
245 with SALL1 in ES cells, but only SALL4 is required for early mammalian development (Miller et
246 al., 2016; Nishinakamura et al., 2001). We therefore created *Sall1*$^{-/-}$*Sall4*$^{FKBP/-}$ ES cells in which
247 one endogenous *Sall4* allele was mutated and the remaining allele was targeted to express a
248 SALL4-FKBP fusion protein.

249 Acute depletion of SALL4-FKBP resulted in rapid and extensive changes in chromatin
250 accessibility as measured using ATAC-seq. Over 18,000 sites showed increased accessibility
251 within 1 hour of SALL4 depletion in *Sall1*$^{(-/-)}$ ES cells (Fig. 4A,B). These sites showed moderate
252 enrichment for SALL4 in undepleted cells, though less than that seen at active enhancers (Fig.
253 4C). When we compared these sites to those showing CHD4-dependent chromatin
254 condensation, we find that only 4559 sites of the more than 52,000 CHD4 -dependent sites
255 also show dependency upon SALL4 to maintain chromatin inaccessibility (Fig. 4D-F). This
256 means that only 17.2% of SALL4-dependent sites also rely on CHD4 to prevent chromatin
257 opening. Moreover, over 47,000 CHD4-dependent sites show neither SALL4 binding nor SALL4
258 dependence to remain inaccessible (Fig4. D-G). Similarly, over 20,000 SALL4-dependent sites
259 show no change in accessibility upon CHD4 depletion, despite showing similar levels of
260 enrichment for NuRD components as those dependent upon both SALL4 and CHD4 (Fig.
261 4E,H). Consistent with the proposed preference of SALL4 for binding to A/T-rich DNA, SALL4-
262 unique regions showed enrichment for SALL4 binding and a high A/T-content (53.9%) (Fig.
263 4D). CHD4-unique regions showed little if any SALL4 enrichment and a much lower A/T
264 content (44.2%), while those sites requiring both SALL4 and CHD4 to remain inaccessible
265 showed enrichment for NuRD components as well as SALL4 and displayed intermediate A/T
266 content (48.2%). Together, these data show that both CHD4 and SALL4 broadly restrict
267 chromatin accessibility across the genome, but that their activities overlap at only a relatively
268 small proportion of sites.

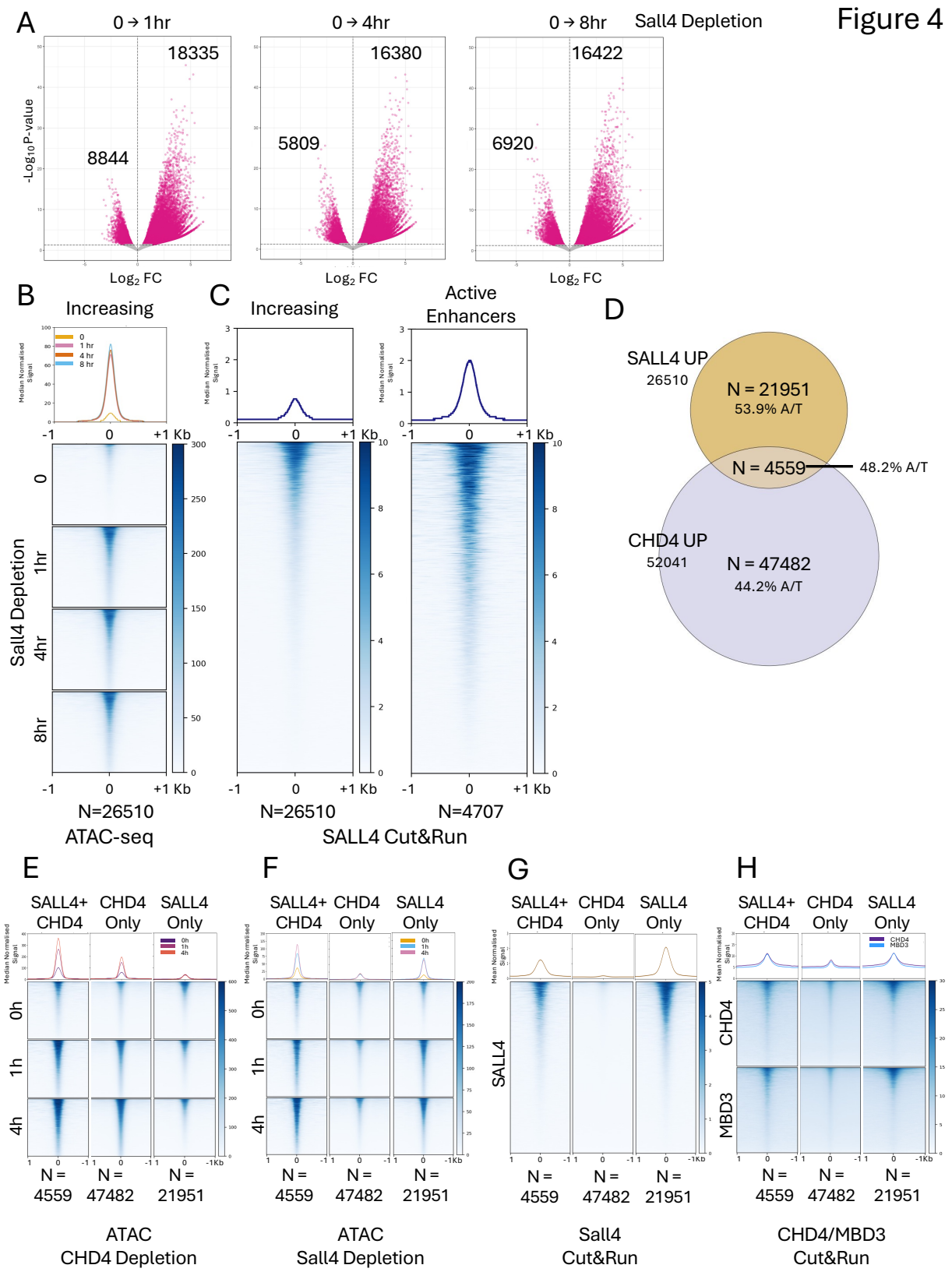

Figure 4. CHD4 and SALL4 both restrict chromatin accessibility. A. Volcano plots of differentially accessible ATAC-seq peaks when comparing 1 hour, 4 hours or 24 hours of SALL4 depletion with those seen in undepleted cells (0). Magenta spots indicate statistically significant differences (FDR > 0.05). Numbers of significant peaks decreased or increased are indicated on the plots. **B**. Heatmaps of ATAC-seq signal for all regions displaying increased accessibility (N=26510) across the SALL4 depletion time course are displayed for each time

point. **C**. Heatmap of SALL4 Cut&Run signal in undepleted ES cells (taken from (Ru et al., 2022)) at all regions displaying increased accessibility across the SALL4 depletion time course (left, N=26510) or at active enhancers (right, N=4339). **D**. Overlap of sites showing increased accessibility upon SALL4 depletion with those increasing upon CHD4 depletion (upDARs). The % A/T base composition of the different categories of sites is indicated. **E, F**. Heatmaps of ATAC-seq signal at sites increasing upon either SALL4 or CHD4 depletion (SALL4+CHD4), sites increasing upon CHD4 depletion but not upon SALL4 depletion (CHD4 Only), or sites increasing upon SALL4 depletion but not upon CHD4 depletion (SALL4 Only) plotted at indicated time points of CHD4 depletion (**E**) and SALL4 depletion (**F**). **G, H**. Cut&Run signal for SALL4 (**G**) or for CHD4 and MBD3 (**H**) in undepleted ES cells at the three different classes of sites. Median curves in **B, C,** and **E-H** are plotted with standard error of the mean in lighter shading.

NuRD limits transcription factor binding to chromatin

Sites decreasing in accessibility upon CHD4 depletion showed an increase in enrichment for both NANOG and SOX2 after 30 minutes, even though these sites were, on average, losing accessibility and losing enrichment for the active chromatin marks H3K4Me1 and H3K27Ac at that time (Fig. 5A,B). Active enhancers similarly showed an increase in NANOG and SOX2 enrichment from 30 minutes of CHD4 depletion (Fig. 5C). An example locus is shown in Figure 5D, where a cluster of enhancers located 50-70Kb downstream of the *Klf4* gene contains several high accessibility sites. Those located at 68, 57 and 55 Kb downstream of *Klf4* (labelled 68, 57 and 55, respectively in Figure 5D) all show a loss of ATAC-seq signal but a gain in NANOG and, to a lesser extent, SOX2 enrichment between 0 and 30 minutes of CHD4 depletion. NANOG enrichment then decreases again at 1 and 4 hours while Sox2 enrichment remains relatively constant, even though accessibility continues to decrease.

The simultaneous decrease in chromatin accessibility and increase in transcription factor enrichment after 30 minutes of CHD4 depletion could indicate that CHD4/NuRD plays a direct role in controlling transcription factor binding to chromatin. To independently assess the impact CHD4 has on transcription factor binding, we used single molecule imaging in live ES cells to directly measure transcription factor binding kinetics upon CHD4 depletion. A HALO-Tag cassette was knocked-in to the endogenous *Nanog*, *Klf4* or *Sox2* loci in the CHD4-mAID ES cell line to create strains expressing the different C-terminal protein fusions. Single HALO-tagged protein molecules were then labelled with a photoactivatable dye (PA-JF646, (Grimm et al., 2016)) and tracked at two distinct temporal regimes where we collected images either every 20 ms or 500 ms, using double-helix point spread function (DH PSF) microscopy as they moved within a 4-μm slice of the nucleus. Recording at a 20 ms time resolution allows the segmentation of trajectories into freely diffusing and chromatin-bound states, and this

314 data can be used to extract the chromatin binding kinetics of proteins and complexes (Basu et
315 al., 2023). Here, we used these data to determine residence times – how long the molecules
316 remain bound to chromatin. The proportion of molecules that remain bound to chromatin
317 after increasing lengths of time was then plotted before and after CHD4 depletion (for 1 hour)
318 and the results were fitted with a single exponential decay to determine the apparent
319 dissociation rate, k_{off} (Fig. 5E). NANOG-HALO, SOX2-HALO and KLF4-HALO all showed a
320 pronounced decrease in apparent k_{off} after CHD4 depletion (Fig. 5F-H), consistent with CHD4
321 actively limiting transcription factor residence times on chromatin.
322 To determine whether it is CHD4 by itself or the intact NuRD complex that can remodel
323 transcription factor binding, we similarly imaged NANOG-HALO and KLF4-HALO in MBD3-
324 depletable ES cells after disruption of the NuRD complex (Fig. 5I). These cells were also null
325 for *Mbd2*, which encodes a protein displaying partial functional redundancy with MBD3 but is
326 dispensable in ES cells (Hendrich et al., 2001). As CHD4 is largely responsible for the binding
327 of NuRD to its target enhancers, removal of MBD3 enables disassembly of NuRD, but does not
328 prevent CHD4 binding to chromatin (Basu et al., 2023; Bornelöv et al., 2018; Zhang et al.,
329 2016). The nucleosome remodelling activity of CHD4 is, however, greatly reduced outside of
330 NuRD (Bornelöv et al., 2018). We therefore reasoned that if it is intact NuRD that is required
331 (as opposed to just CHD4), depletion of MBD3 should also limit TF residence times. Indeed,
332 we detected a significant decrease in the apparent k_{off} of stably bound NANOG-Halo and
333 KLF4-Halo after 1 hour of MBD3 depletion (Fig. 5J,K). We therefore conclude that intact NuRD
334 (and not CHD4 by itself) actively limits transcription factor residence times on chromatin,
335 while at the same time contributing to the maintenance of chromatin accessibility at active
336 regulatory regions.
337

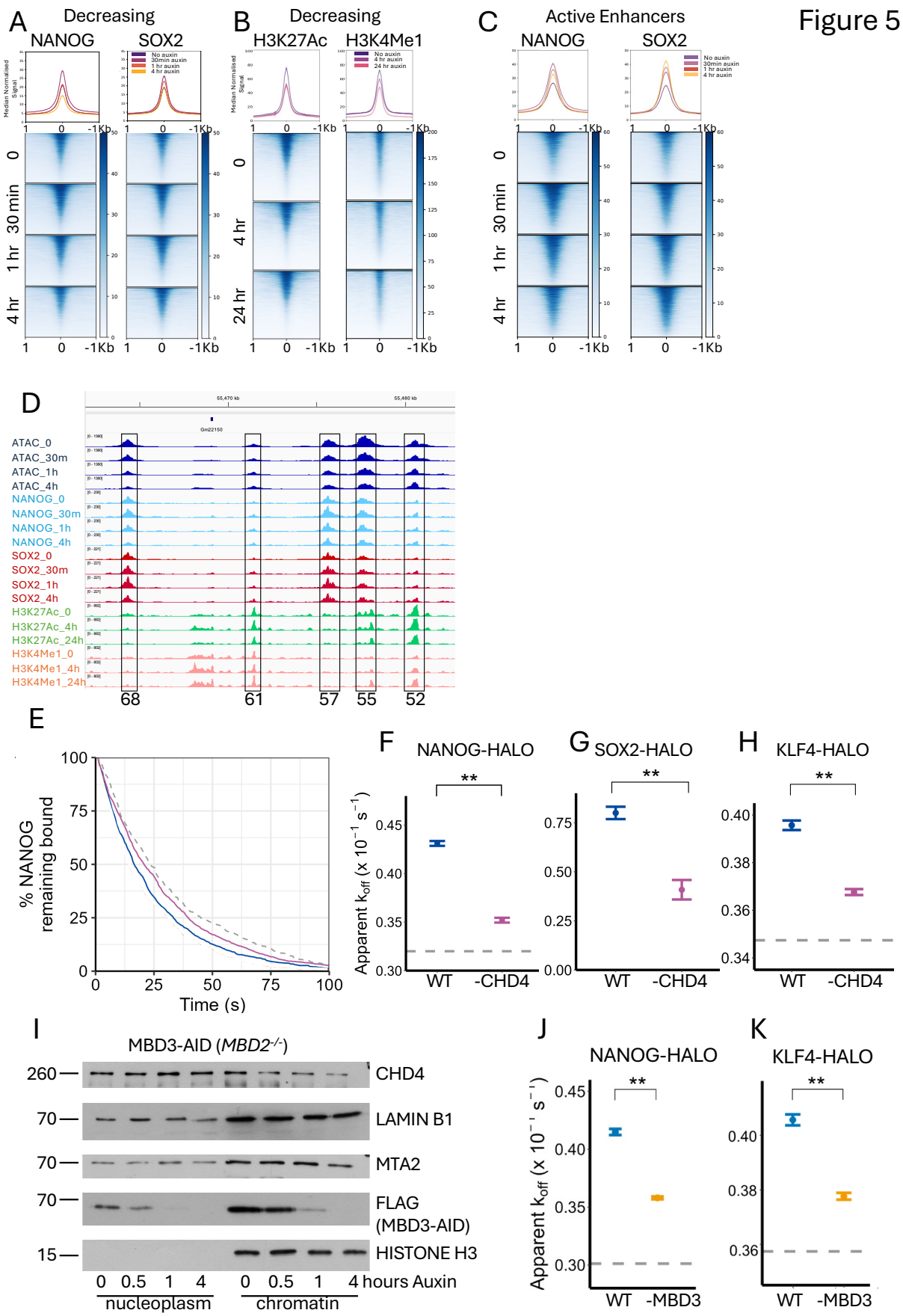

Figure 5. NuRD regulates NANOG and SOX2 binding to active sites. A. Heatmaps of NANOG and SOX2 Cut&Run signal at indicated times of CHD4 depletion across sites decreasing in accessibility (N = 8384). **B**. Heatmaps of H3K27Ac and K3H4Me1 Cut&Tag signal

343 at indicated times of CHD4 depletion across decreasing accessibility sites. **C**. Heatmaps of
344 Cut&Run signal for NANOG and SOX2 across active enhancers (N = 4707) at indicated times
345 of CHD4 depletion. Median curves in **A-C** are plotted with standard error of the mean in lighter
346 shading.**D.** IGV screenshot of the enhancer cluster downstream of the *Klf4* gene displaying
347 ATAC-seq, Cut&Run and Cut&Tag data as indicated at the left. Boxed regions are labelled with
348 the distance in Kb from the annotated *Klf4* transcription start site. **E**. Fluorescence survival
349 curves of chromatin-bound NANOG-HALO molecules in 2iL (blue line) or after 1 hour of CHD4
350 depletion (purple line). The grey dotted line represents the fluorescence survival curve for
351 molecules in a fixed-cell control imaged under identical conditions. **F**. Apparent dissociation
352 rates (k_{off}) of chromatin-bound NANOG molecules calculated through fitting a single
353 exponential decay model to the survival curves in **panel E**. Error bars represent 95%
354 confidence intervals for each fit applied to data taken from three independent experiments.
355 The horizontal dashed line represents the upper 95% confidence limit for a fixed-cell control.
356 ** indicates that 99% confidence intervals do not overlap, i.e. $p < 0.01$. **G.H**. As in **F** but for
357 SOX2 (**G**) and KLF4 (**H**). The fixed cell control was not imaged in the SOX2 experiments in
358 panel **F**. **I**. Western blots of nuclear soluble (Nucleoplasm) and chromatin fractions across
359 MBD3 depletion probed with antibodies directed against the indicated proteins. Times in
360 hours of Auxin addition are indicated across the top. Lamin B1 and Histone H3 act as loading
361 controls. **J, K.** Apparent dissociation rates (k_{off}) for NANOG-HALO (**I**) and KLF4-HALO (**J**) before
362 and after 60 minutes of MBD3 depletion. For calculation of k_{off} the trajectories were pooled
363 from 4 replicates of each time point obtained over 2 days.
364

365 **NuRD activity influences active and inactive regulatory elements differently**

366 We next asked how CHD4 activity could have different impacts on accessibility at different
367 kinds of sequences. Information about the structure of accessible regions can be obtained
368 from ATAC-seq data by quantitating recovered fragments of all sizes and determining the
369 frequency and location of recovered Tn5 integration sites using VPlots, (Henikoff et al., 2011;
370 Schep et al., 2015; Serizay and Ahringer, 2021)(Supplementary Figure 2). Applying this
371 analysis at CHD4 -ondensed sites shows an increase in both Tn5 integrations and in reads
372 corresponding to the nucleosome-free region (NFR) after 30-minutes of CHD4 depletion (Fig.
373 6A,B). After 60 minutes, when CHD4 is almost completely depleted, there is an increase in
374 accessibility generally across the entire site, both of short reads within the NFR but also
375 longer reads (200-300bp) extending from the NFR outwards (Fig. 6B). We conclude that NuRD
376 is acting to restrict accessibility of both the NFR and the flanking nucleosomal DNA (see
377 Supplementary Figure 2) at these sites, consistent with the demonstrated role of CHD4/NuRD
378 in maintaining the density of intact nucleosomes (Bornelöv et al., 2018; Dieuleveult et al.,
379 2016; Moshkin et al., 2012).

380 The example of the *Eomes* locus (Fig. 3F) illustrates that some CHD4-condensed sites
381 show a degree of accessibility in the presence of CHD4, while others show little if any
382 accessibility. To better understand how CHD4 prevents chromatin opening at these two

383 different kinds of sites, we constructed Tn5 integration plots and Vplots from the 1000 CHD4-
384 condensed sites showing the least accessibility in undepleted conditions and from the 1000
385 showing the most accessibility (Fig. 6C-F). Sites showing little or no accessibility in
386 undepleted cells initially show very few reads less than 100bp. The V-plots also show reads of
387 200-300 bp distributed across the regions, again indicative of generally inaccessible
388 chromatin. Loss of CHD4 results in the formation and progressive expansion of an NFR, as
389 well as an increase in longer reads with one end located within the NFR (Fig. 6C,D). The Tn5
390 integration plot does not show a general widening of the NFR over time, indicating that CHD4
391 function is largely focussed on maintaining nucleosome density within a 100-200bp region
392 (Fig. 6C). Sites at which CHD4 activity restricts accessibility at already accessible sites
393 showed a general increase in both small and longer reads as CHD4 was depleted, and a
394 broadening of the existing NFR (Fig. 6 E,F). Together these data are consistent with
395 CHD4/NuRD maintaining chromatin compaction at inactive or low activity enhancers by
396 maintaining nucleosome density.
397 The sites at which CHD4 activity maintains accessibility displayed a prominent NFR as well
398 as high density of longer reads in undepleted cells (Fig. 6G,H). CHD4 depletion induced a
399 general decrease in Tn5 integrations and VPlot signal intensity across these sites, consistent
400 with CHD4 acting to generally maintain accessibility.
401 We next asked why CHD4 promoted accessibility at highly accessible active sites (e.g. Fig.
402 6G,H) but reduced accessibility at slightly less accessible, inactive sites (e.g. Fig. 6E,F). We
403 took advantage of ES cells in which a tamoxifen-inducible MBD3b is expressed in an
404 otherwise *Mbd3*-null ES cell line, allowing us to restore NuRD activity to cells upon tamoxifen
405 addition (Bornelöv et al., 2018; Reynolds et al., 2012). We had previously subjected these
406 cells to micrococcal nuclease (MNase) sequencing at different time points after MBD3
407 induction to show that restoration of NuRD activity caused increased density of intact
408 nucleosomes across sites of active transcription (Bornelöv et al., 2018). Unlike ATAC-seq,
409 sequencing of MNase-treated DNA results in increased reads at sites protected from
410 digestion by bound proteins, i.e. less accessible regions, and a decrease in signal at locations
411 where the DNA is easily accessible and therefore digested by the MNase. In that study, we
412 used an MNase concentration at which DNA associated with intact nucleosomes is protected
413 from MNase digestion. Lower MNase concentrations, however, will recover DNA protected by
414 other chromatin proteins as well as by partial (fragile) nucleosomes (Kubik et al., 2015; Xi et
415 al., 2011).

We therefore subjected cells undergoing the time course of NuRD reformation to lower MNase concentrations prior to sequencing. Traditional MNase sequencing shows that NuRD increases the density of intact nucleosomes at both classes of accessible sites, as indicated by an increase in signal from the red line (NuRD-deficient) to the black line (24h NuRD restored) in the top panels of Figure 6I. This effect is more pronounced at the most accessible inactive sites ("UP Most Accessible", black line, Fig. 6I), occurring across a broader area than at fully active sites ("All Decreasing", black line). The lower MNase concentration, by contrast (Fig. 6I, lower panels) produces a peak of MNase resistance in the absence of NuRD activity at both classes of sites (red lines), indicating an accumulation of structures which are digested by the higher MNase concentration, such as fragile nucleosomes. Restoration of NuRD activity clears the majority of this signal at the most accessible inactive sites, but only moderately reduces their abundance at fully active sites (Fig. 6I, lower panels). These data indicate that at highly active regions, NuRD acts to limit the abundance of fragile nucleosomes and other proteins, while marginally increasing the density of intact nucleosomes, which has an overall result of maintaining these sites in a fully active state. It does not completely remove the fragile nucleosomes from these sites, which are presumably being created by the activity of other chromatin remodellers (Klein et al., 2023; Nocente et al., 2024). In contrast, at accessible but inactive sites it prevents the accumulation of fragile nucleosomes which would otherwise cause further opening and enable activation of inactive regulatory elements. This means that the activity of CHD4 does not differ at the two classes of sites, but it is the presence of other remodellers producing fragile nucleosomes which dictates whether CHD4 activity acts to maintain or prevent accessibility (Fig. 7).

Together, these data show that CHD4 shows two modes of binding on chromatin: in addition to the high enrichment seen at active enhancers and promoters, it also shows low-level binding at silent and/or cryptic regulatory elements across euchromatin. At the former class of sites, it acts to limit the residence times of chromatin-associated proteins to maintain highly accessible chromatin. This maintenance activity of CHD4/NuRD is necessary for the full activity of these elements to direct appropriate transcription of target genes. At the latter class of sites we propose it maintains chromatin in an inaccessible state, preventing accumulation of fragile nucleosomes and preventing transcription factors from recognising and stably binding their cognate motifs and thereby prevents spurious activation of these elements.

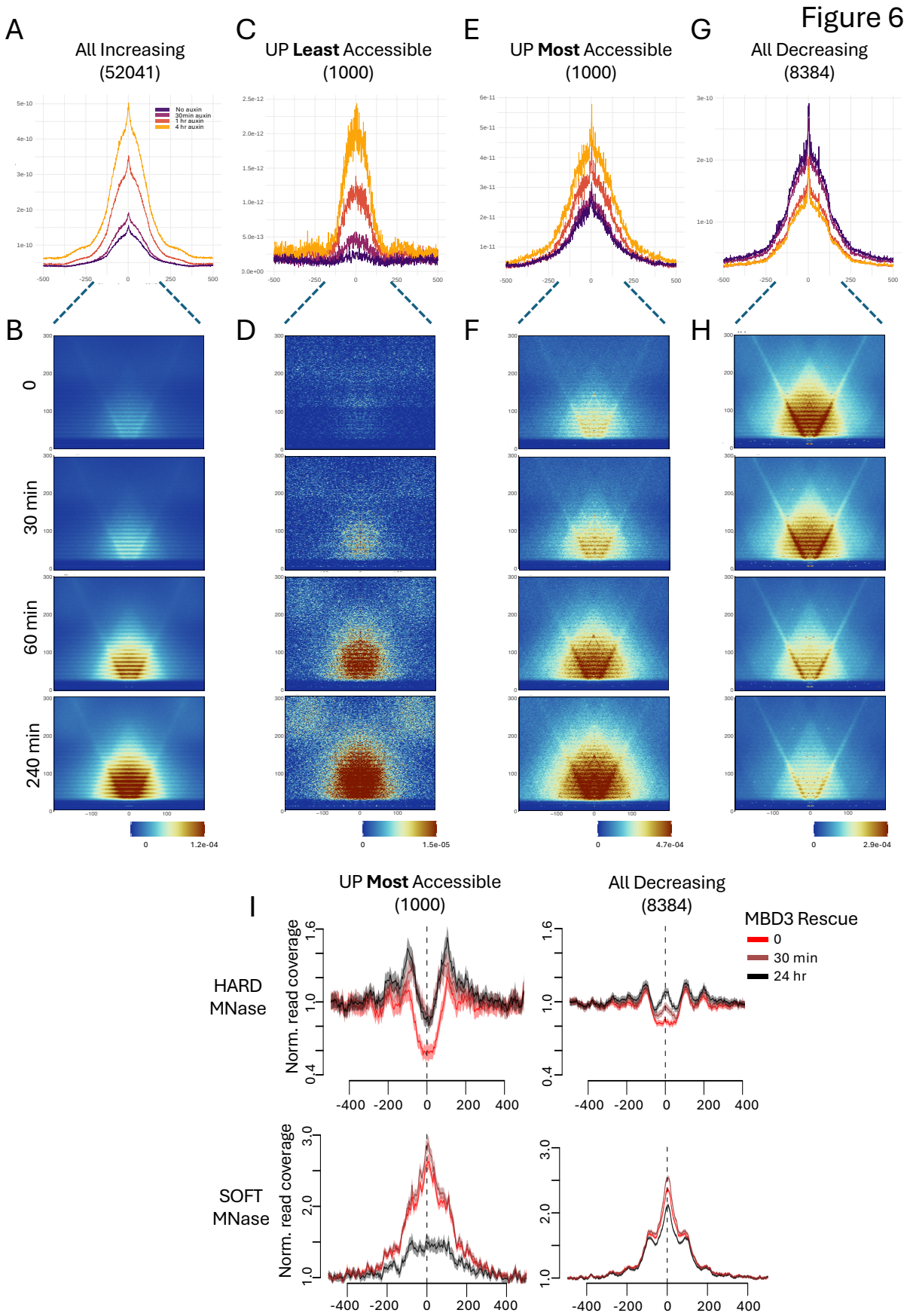

Figure 6. CHD4 controls accessibility differently at different classes of sites. A, C, E, G Tn5 integration frequency was determined from ATAC-seq data and plotted across indicated sites across the CHD4 depletion time course. The number of sites is shown in parentheses. **B, D, F, H** Vplots across sites indicated above (corresponding to the Tn5 integration plots) at

453 indicated times of CHD4 depletion. See **Supplementary Figure 2** for a Vplot schematic. **I.**
454 MNase-seq data collected 0 (red), 30 minutes (dark red) or 24 hours (black) after of NuRD
455 reformation in *Mbd3*$^{-/-}$ ES cells are plotted across indicated sites. Top graphs show results
456 from "Hard" MNase treatment while bottom graphs show "Soft" MNase treatment (see text).
457 The y-axis shows normalised read coverages, while the X-axis shows distance in base pairs
458 from the centre of the feature. Curves show mean and standard error from 3 biological
459 replicates.
460

461 **Discussion**

462 Assessing CHD4 function by traditional knockout experiments is difficult as ES cells
463 without CHD4 undergo cell cycle arrest and begin to apoptose after 24 hours (Fig. 1B). Even
464 with siRNA or inducible deletion, cells in a population will lose CHD4 at different times and, in
465 the case of siRNA, to different extents, making primary function difficult to ascertain. Genetic
466 deletion in mouse ES cells has been used extensively to define protein function in cells and in
467 intact mice. In such an experiment the genetic lesion will often be induced in a single cell, and
468 a clone of cells will be grown out from that single cell. While this is an extremely powerful
469 method for defining gene function, there is usually a very large number of cell divisions
470 occurring and considerable time passing between loss of the gene and assessment of
471 phenotype, making it of limited use when studying proteins required for the viability of ES
472 cells. Resulting phenotypes may be due directly to the absence of protein function but may
473 also reflect adaptations made by cells selected to proliferate in the absence of that protein.
474 The advent of inducible depletion methods (summarised in (Wit and Nora, 2023)) has meant
475 we can now infer protein function by assessing the immediate molecular consequences of
476 loss of a given protein activity in the very short term. Combined with genome-wide profiling,
477 this has allowed us to identify both a novel transcription factor remodelling activity for CHD4
478 and to define how this combines with the protein's nucleosome remodelling activity to exert
479 different functions at different classes of sites.
480 CHD4 is an abundant chromatin remodeller with a well-defined function in moving intact
481 nucleosomes. Here we show that CHD4 can also actively limit the residence times of
482 transcription factors on chromatin. The combination of these two activities has different
483 consequences at different kinds of sequences. At highly accessible, active sites (Fig. 7A)
484 CHD4 enrichment is high and it acts to limit the binding of transcription factors and fragile
485 nucleosomes to regulatory regions, allowing for full accessibility and functionality of these
486 regulatory elements. At inactive, less accessible euchromatic sites (Fig. 7B) CHD4 associates
487 more infrequently, but here it's TF removal activity, combined with maintenance of

488 nucleosome structure, is sufficient to keep accessibility low and to prevent transcription
489 factors from stably binding recognition motifs. This activity is sufficient to prevent the binding
490 of NANOG and SOX2, the latter being capable of binding nucleosomal templates (Dodonova
491 et al., 2020; Zhu et al., 2018). By combining these two activities, CHD4 functions to prevent
492 spurious activation of cryptic and/or silent regulatory regions, thereby reducing
493 transcriptional noise, but also acts to facilitate the activity of highly accessible regulatory
494 regions, allowing cells to accurately and rapidly respond to differentiation cues (Fig. 7).
495 Many transcription factors recognise and bind to specific sequence motifs in DNA. A
496 transcription factor recognising a 7 base pair sequence should, on average, have more than
497 150,000 different potential binding sites in a mammalian genome. Yet ChIP-seq and Cut&Run
498 studies have found most transcription factors associate with orders of magnitude fewer sites
499 in any one cell type (Lambert et al., 2018; Srivastava and Mahony, 2020). Most transcription
500 factors bind preferentially or exclusively in accessible chromatin, so it is believed that
501 differences in chromatin accessibility, or nucleosome positioning across sites, determines
502 which subset of the potential consensus DNA binding motifs are available for TF binding at
503 any given time or cell type (Workman and Buchman, 1993; Zhu et al., 2018). Here we identify
504 CHD4 as one factor which acts to prevent transcription factors, even so-called Pioneer
505 Factors, from binding thousands of sites in inaccessible chromatin. Consistently with this
506 model, CHD4 was found to prevent binding of the GATA3 transcription factor to inappropriate
507 sites in breast cancer cells undergoing mesenchemal-to-epithelial transition (Saotome et al.,
508 2024). We propose that CHD4's chromatin remodelling activity keeps the sites inaccessible,
509 so TF binding is not favoured (i.e. k_{on} is low). The ability of CHD4 to remove TFs from chromatin
510 means that even if they are capable of binding to a nucleosomal substrate, CHD4 promotes
511 their dissociation from chromatin so they are quickly removed (Fig. 7B). At highly accessible
512 chromatin, CHD4 similarly limits TF residence times by increasing k_{off}, however accessibility is
513 high so the k_{on} is also high. We propose that at these sites CHD4 activity balances the high k_{on}
514 by maintaining a high k_{off}, thus facilitating the turnover of bound molecules (Fig. 7A). Without
515 CHD4, k_{off} decreases while k_{on} remains high, resulting in more stable binding of TFs to
516 chromatin. CHD4 and NuRD have been shown to be important for cells to properly respond to
517 differentiation cues in a wide variety of organisms and contexts (Ahringer, 2000; Bracken et
518 al., 2019; Lenz and Brehm, 2023; McDonel et al., 2009; Signolet and Hendrich, 2015) and we
519 propose that by facilitating TF turnover and accessibility at promoters and enhancers, CHD4

520 and NuRD facilitate the ability of regulatory elements to respond to differentiation cues (Fig.
521 7).

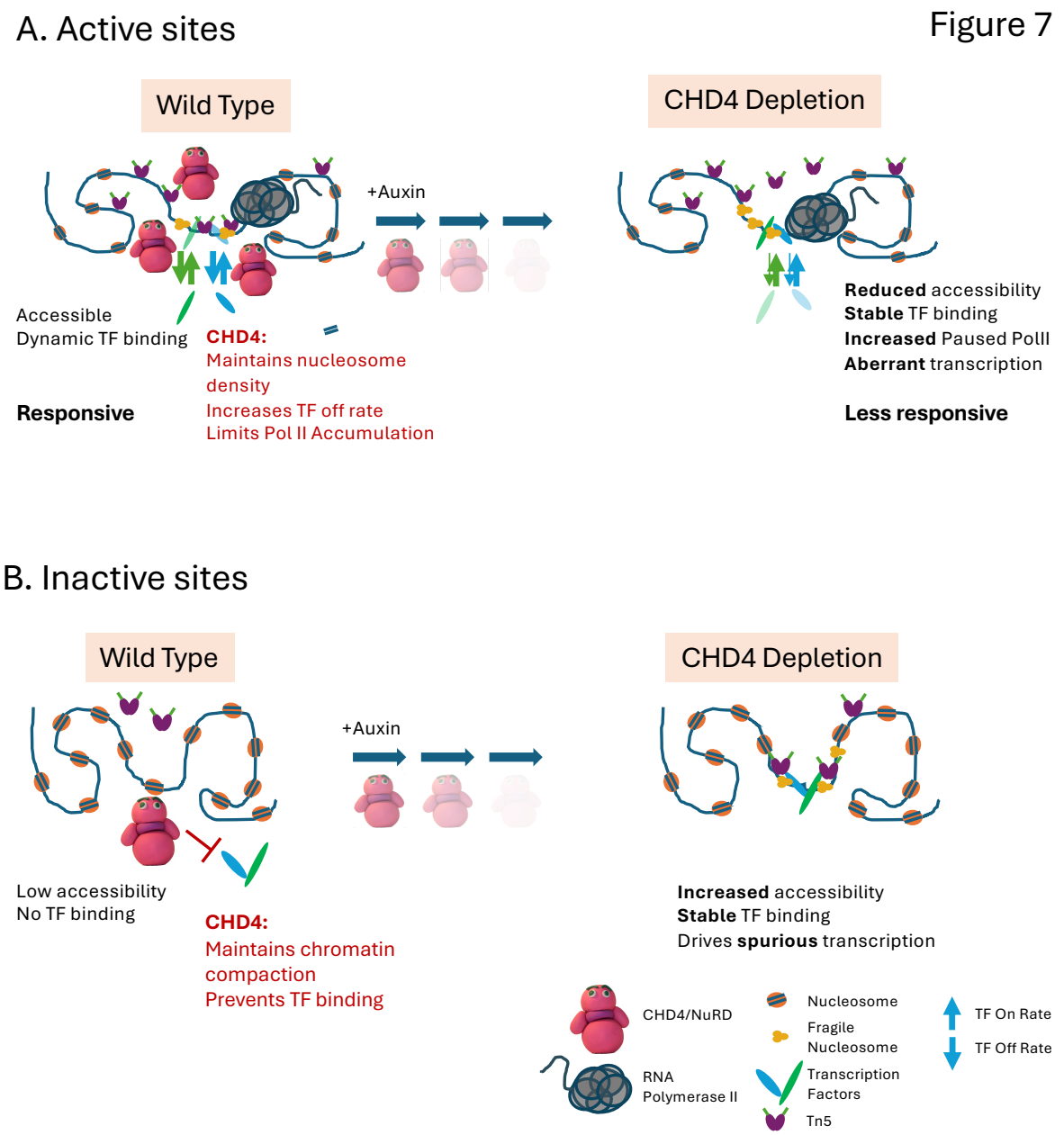

522

523 **Figure 7. Model of CHD4 function. A. Highly accessible sites.** In undepleted cells these
524 sites are extensively bound by CHD4/NuRD, where it acts to promote the off rate of
525 transcription factors to promote accessibility. Tn5 is able to access the central NFR but also
526 can integrate into the flanking nucleosomal DNA. After CHD4 depletion, the on rate for TFs
527 does not change, but the off rate is now much reduced, resulting in increased TF binding. The
528 sites become less accessible to Tn5, such that although it can still access the hypersensitive
529 site within the NFR, there are fewer integrations extending outwards. These regulatory regions
530 cannot quickly respond to receipt of external signals. **B.** Model of CHD4 function at
531 inaccessible, silent enhancers. In undepleted conditions, there is low CHD4 enrichment at
532 these sites. Here, CHD4 acts to prevent binding of transcription factors and maintain low
533 accessibility, such that Tn5 cannot frequently access the DNA. After CHD4 depletion, the
534 locus becomes more accessible, and transcription factors can stably bind. This leads to
535 spurious activation of distal promoters and an increase in transcriptional noise.
536

537 CHD4's activity to prevent spurious TF binding and chromatin opening occurs at many sites
538 where enrichment of CHD4 by ChIP or Cut&Run is low, but not absent. Despite the low
539 amount of CHD4 detected at these sites, this activity was sufficient to prevent activation of
540 silent and cryptic regulatory regions (Fig. 2). This low-level enrichment of CHD4 at sites where
541 it prevents activation could explain an observation made during Drosophila spermatogenesis,
542 where the CHD4 orthologue dMi2 was found to prevent transcription from cryptic promoters,
543 despite not being detected at these promoters by ChIP-seq assays (Kim et al., 2017). A recent
544 study in *S. cerevisiae* found many transcription factors appear to exert influences over
545 expression of genes without detectable association at that gene and bind many sites where
546 they exert no detectable regulatory function (Mahendrawada et al., 2025). While some have
547 argued that one should focus on high confidence binding targets to assess protein function
548 (Mindel and Barkai, 2025), in our case this would have resulted in us ignoring most of the
549 50,000 sites at which we detect CHD4-dependent chromatin compaction (Fig. 1C). While we
550 have argued that chromatin changes detected within 30 minutes are likely to be direct
551 consequences of NuRD manipulations (Fig. 6), we do acknowledge that it is possible these
552 are indirect consequences of loss or gain of NuRD activity. We agree that the definition of
553 "targets" can be highly variable between studies, which is why we preferred to assess CHD4
554 enrichment at subsets of sites where function was identified, irrespective of whether it
555 passed the threshold of being a "peak."
556 SALL4 presents another example of a protein exerting function away from its predominant
557 sites of chromatin enrichment: initial ChIP-seq results indicated that SALL4 was
558 predominantly located at enhancers, whereas more recent Cut&Run data indicates a wider
559 spectrum of sites bound by SALL4 (Kong et al., 2021; Miller et al., 2016; Pantier et al., 2021; Ru
560 et al., 2022). We find that SALL4 shows lower enrichment at A/T-rich genomic sites than it
561 does at enhancers, but that it nevertheless has a major impact on chromatin compaction at
562 these genomic A/T-rich sites (Fig. 4). While many groups, including ours, have generally
563 assumed protein function would be focussed at ChIP-seq "peaks," we argue here that
564 focusing on protein enrichment levels on chromatin is not necessarily the best way to identify
565 important sites of protein activity.
566 Together, our data show that CHD4 exerts functions on chromatin beyond its well-
567 described ability to slide intact nucleosomes along the DNA (Zhang et al., 2016; Zhong et al.,
568 2020). Consistent with this conclusion, a recent paper found that acute depletion of CHD4
569 resulted in an increase in fragile nucleosomes at enhancers (Nocente et al., 2024), while we

570 and others have found that NuRD acts to limit the amount of paused RNA Polymerase II at
571 active promoters (Bornelöv et al., 2018; Pundhir et al., 2023). It is possible that CHD4
572 translocates along the DNA within accessible sequences and displaces any bound proteins,
573 such as transcription factors or fragile nucleosomes, that it encounters. Both transcription
574 factors and fragile nucleosomes are less tightly bound to DNA than intact nucleosomes, so it
575 is possible CHD4's nucleosome remodelling activity results in their displacement, while still
576 sliding intact nucleosomes. CHD4 could also displace transcription factors from preferred
577 binding sites, thus making binding less favourable. Such activity might not be necessary in
578 inaccessible chromatin, but at inactive enhancers showing a small amount of accessibility,
579 infrequent binding and translocation of NuRD across the accessible region could remove any
580 proteins which have managed to bind. Whether this is achieved through a similar ATP-
581 dependent mechanism as is used to slide nucleosomes remains to be determined (Reid et
582 al., 2024; Zhong et al., 2020). Notably, the yeast remodeller INO80 was found to bind
583 differently to fragile nucleosomes vs intact nucleosomes, possibly indicating different
584 mechanisms of remodelling the two different substrates (Wu et al., 2023; Zhang et al., 2023).
585 A recent study showed that the nucleosome remodelling activity of a different remodeller,
586 SMARCA5, is dictated by the density of nucleosomes on the DNA that it encounters: at high
587 density sites it maintains that density, while at low density sites it slides nucleosomes across
588 the DNA to facilitate TF access (Abdulhay et al., 2023). We find that CHD4 increases density
589 of intact nucleosomes at sites where it prevents or maintains accessibility (Fig. 6I, top panels)
590 and also limits TF residence times at both classes of sites. Therefore, unlike SMARCA5, we
591 see no evidence that the activity of CHD4 differs between condensed and accessible
592 chromatin, but rather the consequences of that activity are different at different kinds of sites
593 (Fig. 7).
594 The residence times of transcription factors vary but are generally on the order of a few
595 seconds (Lu and Lionnet, 2021). Why might it be important to limit the residence times of
596 transcription factors? We propose that this could fix an enhancer into a specific state, when
597 one important job of enhancers is to be responsive to changes in stimuli. If no change in
598 status quo is required, then after CHD4 promotes eviction of a particular transcription factor
599 from the enhancer it can continually re-bind and exert its influence over that enhancer.
600 Should signals change, the enhancer needs to be able to remove TFs corresponding to the old
601 signal to make space for determinants of the new signal. In this model, CHD4/NuRD

602 maintains this fluidity of transcription factor interactions, ensuring enhancers are rapidly able
603 to respond immediately upon receipt of differentiation cues.
604
605 **Methods**
606 **Mouse embryonic stem (ES) cells**
607 Mouse ES cells were cultured in 2i+LIF media on gelatin-coated plates (Montibus et al.,
608 2023; Mulas et al., 2019). All cell lines were genotyped and tested for mycoplasma regularly.
609 The CHD4-mAID ES cell line was made in BC8, an F1 hybrid from a C57Black/6 and Mus
610 castaneus cross (40, XY), obtained from Anne Ferguson-Smith (Cambridge). MBD3-AID ES
611 cells were created in 23AF, a primary ES cell line derived from *Mbd2*$^{-/-}$, *Mbd3*$^{Flox/Flox}$ mice (40,
612 XX) in a mixed C57Black/6 and 129/Ola background. Sall4-FKBP cells were created in *Sall1*$^{-/-}$
613 *Sall4*$^{+/-}$ ES cells (Miller et al., 2016).
614 Targeting constructs were made using the AID sequence (Nishimura et al., 2009) or mini-
615 AID (Kubota et al., 2013) amplified from an Oct4-AID plasmid; a gift from José Silva (Bates et
616 al., 2021) . Targeting plasmids using the FKBP protein (Nabet et al., 2018) were made by
617 amplifying FKBP from pLEX_305-C-dTAG; a gift from James Bradner & Behnam Nabet
618 (Addgene plasmid # 91798). Plasmids created as part of this study are available from
619 Addgene: https://www.addgene.org/Brian_Hendrich/.
620 To create Auxin-depletable cell lines, parent lines were first transfected with a PiggyBac
621 construct to constitutively express OsTir1 (created using pMGS56 (GFP-ARF16-PB1-P2A-
622 OsTIR1); a gift from Michael Guertin (Addgene plasmid # 129668)) linked to either G418 or
623 Hygromycin resistance, and cells were cultured under selection to maintain OsTir1
624 expression. To create degron knock-ins, cells were lipofected with a targeting vector and
625 appropriate gRNA (Table 1) in a Cas9-expression vector (pSpCas9(BB)-2A-GFP (PX458); a gift
626 from Feng Zhang; Addgene plasmid # 48138). Drug resistant colonies were genotyped and
627 correctly targeted clones were subsequently transiently transfected with an expression
628 plasmid for Dre recombinase to remove ROXed drug selection cassettes. *Chd4* targeting
629 required two rounds of transfection, selection, and drug removal, while *Mbd3* and *Sall4*
630 targeting required one round. For protein depletion, cells were treated with 500 μM Auxin or
631 500 μM dTAG-13 in standard culture media. All HALOTag-fusion ES cell lines were
632 heterozygous for the HALOTag fusion, i.e. HALO/+, and verified by western blotting.
633
634

Gene	gRNA	Sequence (5' -- 3')
Chd4	gRNA1	GGTGGAGGTGGATATCACTC
Mbd3 A3xF	gRNA1	TTCTCACGCGTCACTCGCTC
Mbd3	gRNA2	CAGCCATTCCCTGGAAGTAC
Sall4	gRNA1	AATAAGATTGCTGTCAGCTA
Sall4	gRNA2	AAGATTGCTGTCAGCTAAGG
Nanog	gRNA1	AACTACTCTGTGACTCCACC
Sox2	gRNA1	TGCCCCTGTCGCACATGTGA
Klf4	gRNA2	GTGGGTCACATCCACTACGT

Table 1. gRNA sequences used for gene targeting

Nuclear extract fractionation and western blotting

Nuclear fractionation was carried out as described (Gillotin, 2018). Briefly, cells were collected in ice-cold PBS and pelleted in a refrigerated centrifuge. The cell pellet was lysed by gentle up and down pipetting five times in ice-cold buffer E1 (50 mM HEPES, 140 mM NaCl, 1 mM EDTA, 10% glycerol, 0.5% NP40, 0.25% Triton X-100, 1 mM DTT, protease inhibitors). After pelleting and washing in E1 buffer, the pellet was resuspended in ice-cold E2 buffer (10 mM Tris-HCl, 200 mM NaCl, 1 mM EDTA, 0.5 mM EGTA, protease inhibitors) and shaken for 45 minutes at 1400rpm at 4°C. The supernatant, representing the nuclear fraction, was collected into a fresh tube. After washing in E2 buffer, the pellet was resuspended in ice-cold E3 buffer (50 mM Tris-HCl, 20 mM NaCl, 1 mM MgCl2, 1% NP-40, protease inhibitors). The resuspended pellet was sonicated at 4°C in a Bioruptor Plus (Diagenode) for 5 minutes, using 30-second ON/30-second OFF cycles at high power. Following sonication, nuclear and chromatin fractions were centrifuged at 16,000xg at 4°C for 10 minutes. 10 µg of extract per lane was used for western blots. Antibodies are listed in Table 2.

Antibody target	Raised in	Supplier	Cat #	Dilution (WB)
CHD4	Mouse	Abcam	ab70469	1/5000
CHD4	Rabbit	Abcam	ab72418	1/10000
FLAG	Mouse	Sigma Aldrich	F3165/F1804	1/2000

HA	Mouse	Invitrogen	26183	1/2000
ADNP	Goat	R&D Systems	AF5919	1/2000
Histone H3	Rabbit	Abcam	ab1791	1/5000
MTA2	Mouse	Abcam	ab50209	1/5000
NANOG	Rabbit	Bethyl Labs	A300-387A	1/2000
SOX2	Rat	E-bioscience	14-9811-82	1/2000
Lamin B1	Rabbit	Abcam	ab133741	1/10000
Mouse IgG	Rabbit	Invitrogen	A16162	1/100
Rabbit IgG	Guinea Pig	Antibodies Online	ABIN101961	1/100
Goat IgG	Rabbit	Abcam	ab6697	1/100
Rat IgG	Rabbit	Abcam	ab6703	1/100
Mouse IgG	Sheep	VWR	NA931V	1/2000
Rabbit IgG	Donkey	VWR	NA934V	1/2000

Table 2. Antibodies used in this study with dilutions used for western blot.

Cell cycle analysis

The cell cycle distributions of auxin (500 μM) or dTAG-13 (500 nM) treated ES cell lines were assessed using propidium iodide (PI) staining coupled with flow cytometry. Approximately 200,000 single cells were fixed using 70% ethanol for at least 24 hours before staining. Fixed samples were washed twice in PBS and resuspended in 200 μL of PI solution [50 μg/mL propidium iodide (Invitrogen, P3566) and 50 μg/mL DNase and protease-free RNase A (ThermoScientific, EN0531), diluted in sterile PBS and incubated overnight at 4°C in the dark. The fluorescent intensity of stained samples was determined using the Attune NxT (Thermofisher) equipped with a 561 nm laser line and a minimum of 10,000 single cell events were recorded. The resulting FCS files were analysed using FlowJo (v10.10) and tested for significance using a mixed-effects model with Dunnett's multiple comparisons correction.

Single molecule imaging

ES cells were passaged 24 hours before imaging onto either: No 1.0 35 mm glass bottom dishes (MatTek Corporation P35G-1.0-14-C) or No 1.5 35 mm glass bottom dishes (MatTek Corporation P35G-1.5-14-C) with their surfaces pre-coated in poly-L-ornithine (Sigma Aldrich P4957) for ≥30 minutes at 37°C, followed by three PBS rinses at room temperature, followed by 100µg/ml Laminin (Sigma Aldrich L2020) coating in PBS for >4 hours at room temperature. Cells were labelled on the day of imaging with either 250 nM HaloTag®-PA-JF646 (a gift from L. Lavis, Janelia) for 15 minutes, rinsed twice in PBS and incubated for 20 minutes at 37°C in fresh media. PBS rinsing and 20-minute incubation steps were repeated five more times, and the cells were then imaged in fresh media.

Single-molecule tracking was carried out using oblique illumination (Tokunaga et al., 2008) on a custom-built double helix point spread function microscope with a Nikon Eclipse Ti-U inverted microscope body and a box incubator set to 37°C (Carr et al., 2017). Beams were expanded and collimated using Galilean beam expanders, then combined using dichroic mirrors. For 2D imaging, a Nikon 1.49 NA 60× oil immersion objective (CFI Apochromat TIRF 60XC Oil) was used to focus excitation beams onto the sample, and the microscope was also set to an internal magnification of 1.5x. For 3D DHPSF imaging, a Nikon 1.27 NA 60x water immersion objective lens (CFI SR Plan Apo IR 60XC WI) was used without internal 1.5x magnification. The emission path of the microscope was also modified to include a fixed double helix phase mask (DoubleHelix, Boulder, CO) in the Fourier domain of the emission path of the microscope (Carr et al., 2017; Pavani et al., 2009) . For long-exposure imaging, control samples were fixed in 4% formaldehyde (v/w) in PBS for 10 minutes at room temperature, rinsed twice with PBS and stored in PBS. Samples were imaged in identical pre-warmed culture media and under identical conditions to live-cell samples. Across all experiments, three separate samples per condition were imaged in a day and all experiments were repeated on at least two separate days for biological replications.

Background subtraction with a five-pixel rolling ball radius was carried out on image stacks using open-source software Fiji (Schindelin et al., 2012). Single molecules imaged in 2D were localised using the PeakFit tool within the GDSC Single Molecule Light Microscopy (SMLM) plugin (https://github.com/aherbert/gdsc-smlm (Etheridge et al., 2022)) for Fiji. Localisations were filtered for precision better than 25 nm. For single molecules imaged in 3D, PeakFit was used as above but with an initial precision threshold of 40 nm and an additional analysis step after this. 2D localisations of DHPSF lobes were paired to generate 3D localisations using DHPSFU (https://github.com/TheLaueLab/DHPSFU). Localisations were then tracked across

frames to generate trajectories using custom Python code (https://github.com/wb104/trajectory-analysis). Localisations were connected between two successive frames if they were located within 400 nm of each other.

Short-exposure trajectories were segmented into confined and unconfined sub-trajectories using the 4P-algorithm from (Basu et al., 2023). Bound fractions were calculated for a sample based on the number of trajectory frames assigned as being confined, divided by the total number of trajectory frames. Tracks with a residence time shorter than 1.5 seconds were filtered out to reduce the impact of noise on further analysis. The decay curve of residence times for each sample was fitted to a single exponential fit using MATLAB (2018) to yield apparent dissociation rates. The measured apparent dissociation rate (${k_{off}}^{app}$) was calculated by fitting a single exponential decay function to the survival (Kaplan-Meier) function (S) of TF dwell times measured from the point of first observation (t), as below:

$$S = e^{-{k_{off}}^{app} t}$$

RNAseq

Cells were harvested in Trizol Reagent and RNA purified using Zymo Direct-zol columns (Zymo Research) according to manufacturer's instructions. 60-100 ng of Ribosomal RNA-depleted mRNA was used for library preparation with the the NEXTflex RapidDirectional RNA-seq kit (Illumina). 100 bp paired end (2 x 50 bp) sequencing was performed on a NovaSeq S1 flowcell at the CRUK Cambridge Institute sequencing facility.

Raw data were trimmed using TrimGalore v0.6.4. Reads were indexed and aligned to the unmasked GRC38/mm10 reference genome using the Burrows-Wheeler Aligner (BWA) (Li and Durbin, 2009) . Successful removal of adapter and low-quality bases was assessed using FastQC after trimming. File conversion, sorting, removal of duplicates and mitochondrial reads were performed using samtools (Li et al., 2009) .

Read counts for genomic features were summarised using featureCounts (Liao et al., 2014) and a list of the GRC38/mm10 genomic features in a GTF format downloaded from https://www.ensembl.org/ and https://genome.ucsc.edu/cgi-bin/hgTables. Differential expression was analysed using DESeq2 (Love et al., 2014) . Raw expression counts were transformed and normalised to FPKM (fragments per kilobase of transcript per million mapped reads). Simple linear models were used for pairwise comparative analyses between the 0-timepoint and depletion timepoints. An adjusted p-value threshold of 0.05 was used to

identify significantly differentially expressed genes. For principal component analysis (PCA) and the generation of correlation matrices vst-transformed data were used within DESeq2.

Genes were labelled with their Ensembl and their common gene symbols using the Annotation Hub and ensembldb packages (Rainer et al., 2019) . The ComplexHeatmap package was used for the generation of expression heatmaps (Gu et al., 2016) . Volcano plots were generated using the EnhancedVolcano package. To find enriched gene ontology terms among differentially expressed genes, the enrichGO function of the clusterProfiler R package and the genome-wide annotations were retrieved using the biomaRt package (Yu et al., 2012) .

ATAC-seq

100,000 nuclei were used for each reaction using the OMNI-ATAC protocol (Corces et al., 2017) with 10,000 rat nuclei added as a spike-in control. Tagmentation was achieved using Tn5 made in-house (Picelli et al., 2014) for 30 minutes at 37°C on a shaking block. Immediately after incubation DNA was purified using a Zymo DNA Clean and Concentrator Kit (Zymo Research). DNA was then eluted in 21 µL of DNAse/RNAse-free H2O. Barcoding for library preparation was performed by PCR amplification using NEBNext® High-Fidelity 2X PCR Master Mix (New England Biolabs) and NEBNext® index primers for Illumina sequencing. Amplified samples were purified using AMPure SPRI beads (VWR International Ltd) and resuspended in 25 µL of 10mM Tris-HCl pH 8.0. The Agilent 4200 TapeStation System with D1000 ScreenTape and D1000 Reagents (Agilent) was used for quantification and fragmentation check of the samples. Equimolar ratios of all samples (7 conditions x 2 biological replicates x 2 technical replicates each) were pooled for 300 bp paired end (2 x150 bp) sequencing performed on a NovaSeq S2 flowcell with the CRUK Cancer Institute sequencing facility.

Raw data were trimmed to remove adapter contamination using TrimGalore v0.6.4. Reads were aligned to the GRC38/mm10 reference genome and the Rattus norvegicus/Rnor_6.0 genome (spike-in) using the BWA aligner. File conversion, sorting, removal of duplicates and mitochondrial reads were performed using SAMtools (Li et al., 2009) . Fragments up to 120 bp in length, which represent nucleosome free regions, were used for further analysis. For visualisation purposes bigwig files were generated using bamCoverage from deepTools (Ramírez et al., 2014) . A scale factor was applied calculated as the number of uniquely mapped rat spike-in reads for each sample divided by the number of uniquely mapped reads in the sample with the lowest count. All replicates were pooled together into a single track

765 using bigWigMerge from UCSC Tools (Kent et al., 2002) . Mean profiles of the signal and
766 heatmaps of these regions were plotted using the ComputeMatrix, plotHeatmap and
767 plotProfile functions from deepTools.
768 Peak calling was performed for ≤120bp fragments using macs2 (Zhang et al., 2008) and
769 applying the -f BAMPE -q 0.05 –nolambda –keep-dup auto parameters. Peak annotation and
770 motif analysis was conducted using the annotatePeaks and findMotifsGenome functions
771 from HOMER (Heinz et al., 2010). Integration of these annotated peaks with RNA-seq gene
772 expression data was conducted using custom R scripts. Differential accessibility analysis was
773 carried out using DiffBind (https://bioconductor.org/packages/DiffBind). Differentially
774 accessible regions were identified in pairwise comparisons to timepoint-0 using the rat
775 aligned reads as a spike-in and an adjusted p-value threshold of 0.05. Chromatin state
776 enrichment analysis for both ADNP and CHD4 differentially accessible regions was
777 performed using ChromHMM (Ernst and Kellis, 2017) , using a predefined chromatin state
778 model generated from E14 mouse ESCs ChIP-seq data (Pintacuda et al., 2017) .
779 To analyse the Tn5 integration sites of the ATAC-seq data the plotFootprint() function in
780 VplotR (Serizay and Ahringer, 2021) was used with the addition of a code in a loop to calculate
781 the normalised version of the cuts by manually dividing by the library size of each merged bam
782 file. To analyse the fragment sizes of the ATAC-seq data that correspond to different
783 nucleosome structure sizes, the plotVmat() function in VplotR was used. The merged reads of
784 different time points of CHD4 depletion were normalised using the native libdepth+nloci
785 option, which normalises the reads using the library depth and the number of loci.
786
787 **Cut&Run and Cut&Tag**
788 Cut&Run and Cut&Tag were carried out as described (Janssens et al., 2022; Meers et al.,
789 2019). For Cut&Run 100,000 live ES cells were used per reaction, with 10,000 rat nuclei added
790 as a spike-in control. Cut&Tag was performed on 100,000 nuclei per reaction. Antibodies
791 (Table 2) were used at 1/100 dilution. pAG-MNAse and pA-Tn5 were made and purified in-
792 house as described (Kaya-Okur et al., 2019; Meers et al., 2019). Plasmids 3XFlag-pA-Tn5-Fl
793 and pAG/MNase were a gift from Steven Henikoff (Addgene plasmids #124601 and #123461,
794 respectively). Library preparation for sequencing was carried out in the CSCI Genomics
795 facility. 300 bp paired-end sequencing was performed on a NovaSeqX 25B flowcell at the
796 CRUK Cancer Institute sequencing facility.

797 Raw data were trimmed to remove adapter contamination using TrimGalore v0.6.4. Reads
798 were aligned to the unmasked GRC38/mm10 reference genome and the Rattus
799 norvegicus/Rnor_6.0 genome (spike-in) using the BWA. File conversion, sorting, removal of
800 duplicates and mitochondrial reads were performed using SAMtools. For visualisation
801 purposes bigwig files were generated using bamCoverage from deepTools. A scale factor was
802 applied calculated as the number of uniquely mapped rat spike-in reads for each sample
803 divided by the number of uniquely mapped reads in the sample with the lowest count. All
804 replicates were pooled together into a single track using bigWigMerge from UCSC Tools. Mean
805 profiles of the signal and heatmaps of these regions were plotted from these tracks using the
806 ComputeMatrix, plotHeatmap and plotProfile functions from deepTools. Peak calling was
807 performed using macs2 and SEACR (Meers et al., 2019) . SEACR was used in non-control
808 mode with the stringent threshold setting (threshold = 0.01). Input BED files consisted of
809 scaled fragment bedgraphs generated from CUT&RUN data. Scaling was performed using a
810 factor based on the number of uniquely mapped rat spike-in reads for each sample, which
811 was then adjusted relative to the sample with the fewest mapped reads. Motif analysis was
812 conducted using HOMER. Differential accessibility analysis was also carried out using the
813 DiffBind package, incorporating DESeq2 functionality. Differentially bound peaks were
814 identified in pairwise comparisons to timepoint-0 using an adjusted p-value threshold of 0.05.
815 Chromatin state enrichment analysis for differentially bound regions was performed using
816 ChromHMM as for ATAC-seq.
817
818 **MNase-seq**
819 All MNase experiments, sequencing and data processing were carried out exactly as
820 described (Bornelöv et al., 2018) except that nuclei were digested with 500 U/ml micrococcal
821 nuclease (New England Biolabs) at 24°C for 15 minutes with shaking.
822
823 **Accession numbers**
824 ATAC-seq: E-MTAB-15037
825 RNAseq: E-MTAB-15102
826 nascent RNAseq: E-MTAB-15127
827 Cut&Run: E-MTAB-15606, E-MTAB-15607
828 Cut&Tag: E-MTAB-15625
829 Sall4 Depletion ATAC-seq: E-MTAB-15375

Sall4 Cut&Run: GSE203303 (Ru et al., 2022)

MNase: E-MTAB-6807 (Bornelöv et al., 2018), PRJNA1332303

Acknowledgments

We are grateful to Nick Owens, Vladimir Teif, Joel Mackay and past and present Hendrich and Laue group members for helpful discussions; to David Klenerman and Ziwei Zhang for help with imaging; to Marco Trizzino for support and to the CSCI facilities for expert technical assistance.

Funding

This work was supported by PhD studentships from Wolfson College, Cambridge to A.K., from AstraZeneca to O.O. and from the Medical Research Council to D.S., and by grants from the Medical Research Council to B.D.H. (MR/X018342/1 and MR/Y000595/1) and to E.D.L. (MR/P019471/1 and MR/M010082/1), from the Wellcome Trust to E.D.L. (206291/Z/17/Z), from the Isaac Newton Trust to B.D.H. (17.24(aa)), and core funding from the Wellcome/MRC (203151/Z/16/Z) to the Cambridge Stem Cell Institute.

Author Contributions

AK, OO, IMB, DS and BH created and validated ES cell lines; AK, OO and NR generated sequencing data; AK, OO and RR analysed sequencing data; DS and EDL conducted single molecule imaging experiments and analyses; ML devised methodology; NR, RR, EDL and BH supervised the project and EDL and BH obtained funding. The manuscript was written by BH with input from all other authors.

Competing Interests Statement

The authors declare no competing interests.

Rererences

Abdulhay NJ, Hsieh LJ, McNally CP, Ostrowski MS, Moore CM, Ketavarapu M, Kasinathan S, Nanda AS, Wu K, Chio US, Zhou Z, Goodarzi H, Narlikar GJ, Ramani V. 2023. Nucleosome density shapes kilobase-scale regulation by a mammalian chromatin remodeler. *Nat Struct Mol Biol* 1–11. doi:10.1038/s41594-023-01093-6

Ahringer J. 2000. NuRD and SIN3 histone deacetylase complexes in development. *Trends Genet* **16**:351–356. doi:10.1016/s0168-9525(00)02066-7

Arends T, Dege C, Bortnick A, Danhorn T, Knapp JR, Jia H, Harmacek L, Fleenor CJ, Straign D, Walton K, Leach SM, Feeney AJ, Murre C, O'Connor BP, Hagman JR. 2019. CHD4 is essential for transcriptional repression and lineage progression in B lymphopoiesis. *Proc National Acad Sci* **116**:201821301. doi:10.1073/pnas.1821301116

Aughey GN, Forsberg E, Grimes K, Zhang S, Southall TD. 2023. NuRD-independent Mi-2 activity represses ectopic gene expression during neuronal maturation. *EMBO Rep* **24**:e55362. doi:10.15252/embr.202255362

Basu S, Shukron O, Hall D, Parutto P, Ponjavic A, Shah D, Boucher W, Lando D, Zhang W, Reynolds N, Sober LH, Jartseva A, Ragheb R, Ma X, Cramard J, Floyd R, Balmer J, Drury TA, Carr AR, Needham L-M, Aubert A, Communie G, Gor K, Steindel M, Morey L, Blanco E, Bartke T, Croce LD, Berger I, Schaffitzel C, Lee SF, Stevens TJ, Klenerman D, Hendrich BD, Holcman D, Laue ED. 2023. Live-cell three-dimensional single-molecule tracking reveals modulation of enhancer dynamics by NuRD. *Nat Struct Mol Biol* **30**:1628–1639. doi:10.1038/s41594-023-01095-4

Bates LE, Alves MRP, Silva JCR. 2021. Auxin-degron system identifies immediate mechanisms of OCT4. *Stem Cell Rep* **16**:1818–1831. doi:10.1016/j.stemcr.2021.05.016

Bornelöv S, Reynolds N, Xenophontos M, Gharbi S, Johnstone E, Floyd R, Ralser M, Signolet J, Loos R, Dietmann S, Bertone P, Hendrich B. 2018. The Nucleosome Remodeling and Deacetylation Complex Modulates Chromatin Structure at Sites of Active Transcription to Fine-Tune Gene Expression. *Mol Cell* **71**:56-72.e4. doi:10.1016/j.molcel.2018.06.003

Bracken AP, Brien GL, Verrijzer CP. 2019. Dangerous liaisons: interplay between SWI/SNF, NuRD, and Polycomb in chromatin regulation and cancer. *Gene Dev* **33**:936–959. doi:10.1101/gad.326066.119

Burgold T, Barber M, Kloet S, Cramard J, Gharbi S, Floyd R, Kinoshita M, Ralser M, Vermeulen M, Reynolds N, Dietmann S, Hendrich B. 2019. The Nucleosome Remodelling and Deacetylation complex suppresses transcriptional noise during lineage commitment. *EMBO J* **38**:e100788. doi:10.15252/embj.2018100788

Carr AR, Ponjavic A, Basu S, McColl J, Santos AM, Davis S, Laue ED, Klenerman D, Lee SF. 2017. Three-Dimensional Super-Resolution in Eukaryotic Cells Using the Double-Helix Point Spread Function. *Biophys J* **112**:1444–1454. doi:10.1016/j.bpj.2017.02.023

Corces MR, Trevino AE, Hamilton EG, Greenside PG, Sinnott-Armstrong NA, Vesuna S, Satpathy AT, Rubin AJ, Montine KS, Wu B, Kathiria A, Cho SW, Mumbach MR, Carter AC, Kasowski M, Orloff LA, Risca VI, Kundaje A, Khavari PA, Montine TJ, Greenleaf WJ, Chang HY. 2017. An improved ATAC-seq protocol reduces background and enables interrogation of frozen tissues. *Nat Methods* **14**:959–962. doi:10.1038/nmeth.4396

Dieuleveult M de, Yen K, Hmitou I, Depaux A, Boussouar F, Dargham DB, Jounier S, Humbertclaude H, Ribierre F, Baulard C, Farrell NP, Park B, Keime C, Carrière L, Berlivet S, Gut M, Gut I, Werner M, Deleuze J-F, Olaso R, Aude J-C, Chantalat S, Pugh BF, Gérard M. 2016. Genome-wide nucleosome specificity and function of chromatin remodellers in ES cells. *Nature* **530**:113–116. doi:10.1038/nature16505

904 Dodonova SO, Zhu F, Dienemann C, Taipale J, Cramer P. 2020. Nucleosome-bound SOX2 and
905 SOX11 structures elucidate pioneer factor function. *Nature* **580**:669–672.
906 doi:10.1038/s41586-020-2195-y

907 Ernst J, Kellis M. 2017. Chromatin-state discovery and genome annotation with ChromHMM.
908 *Nat Protoc* **12**:2478–2492. doi:10.1038/nprot.2017.124

909 Etheridge TJ, Carr AM, Herbert AD. 2022. GDSC SMLM: Single-molecule localisation
910 microscopy software for ImageJ. *Wellcome Open Res* **7**:241.
911 doi:10.12688/wellcomeopenres.18327.1

912 Feng Q, Zhang Y. 2001. The MeCP1 complex represses transcription through preferential
913 binding, remodeling, and deacetylating methylated nucleosomes. *Gene Dev* **15**:827–832.
914 doi:10.1101/gad.876201

915 Gillotin S. 2018. Isolation of Chromatin-bound Proteins from Subcellular Fractions for
916 Biochemical Analysis. *BIO-Protoc* **8**:e3035. doi:10.21769/bioprotoc.3035

917 Gómez-del Arco P, Perdiguero E, Yunes-Leites PS, Acín-Pérez R, Zeini M, Garcia-Gomez A,
918 Sreenivasan K, Jiménez-Alcázar M, Segalés J, López-Maderuelo D, Ornés B, Jiménez-
919 Borreguero LJ, D'Amato G, Enshell-Seijffers D, Morgan B, Georgopoulos K, Islam ABMMK,
920 Braun T, de la Pompa JL, Kim J, Enriquez JA, Ballestar E, Muñoz-Cánoves P, Redondo JM.
921 2016. The Chromatin Remodeling Complex Chd4/NuRD Controls Striated Muscle Identity
922 and Metabolic Homeostasis. *Cell Metab* **23**:881–892. doi:10.1016/j.cmet.2016.04.008

923 Gourisankar S, Krokhotin A, Wenderski W, Crabtree GR. 2024. Context-specific functions of
924 chromatin remodellers in development and disease. *Nat Rev Genet* **25**:340–361.
925 doi:10.1038/s41576-023-00666-x

926 Grimm JB, English BP, Choi H, Muthusamy AK, Mehl BP, Dong P, Brown TA, Lippincott-
927 Schwartz J, Liu Z, Lionnet T, Lavis LD. 2016. Bright photoactivatable fluorophores for
928 single-molecule imaging. *Nat Methods* **13**:985–988. doi:10.1038/nmeth.4034

929 Gu Z, Eils R, Schlesner M. 2016. Complex heatmaps reveal patterns and correlations in
930 multidimensional genomic data. *Bioinformatics* **32**:2847–2849.
931 doi:10.1093/bioinformatics/btw313

932 Heinz S, Benner C, Spann N, Bertolino E, Lin YC, Laslo P, Cheng JX, Murre C, Singh H, Glass
933 CK. 2010. Simple Combinations of Lineage-Determining Transcription Factors Prime cis-
934 Regulatory Elements Required for Macrophage and B Cell Identities. *Mol Cell* **38**:576–589.
935 doi:10.1016/j.molcel.2010.05.004

936 Hendrich B, Guy J, Ramsahoye B, Wilson VA, Bird A. 2001. Closely related proteins MBD2 and
937 MBD3 play distinctive but interacting roles in mouse development. *Gene Dev* **15**:710–723.
938 doi:10.1101/gad.194101

939 Henikoff JG, Belsky JA, Krassovsky K, MacAlpine DM, Henikoff S. 2011. Epigenome
940 characterization at single base-pair resolution. *Proc National Acad Sci* **108**:18318–18323.
941 doi:10.1073/pnas.1110731108

942 Hota SK, Bruneau BG. 2016. ATP-dependent chromatin remodeling during mammalian
943 development. *Development* **143**:2882–2897. doi:10.1242/dev.128892

944 Janssens DH, Otto DJ, Meers MP, Setty M, Ahmad K, Henikoff S. 2022. CUT&Tag2for1: a
945 modified method for simultaneous profiling of the accessible and silenced regulome in
946 single cells. *Genome Biol* **23**:81. doi:10.1186/s13059-022-02642-w

947 Kaya-Okur HS, Wu SJ, Codomo CA, Pledger ES, Bryson TD, Henikoff JG, Ahmad K, Henikoff S.
948 2019. CUT&Tag for efficient epigenomic profiling of small samples and single cells. *Nat*
949 *Commun* **10**:1930. doi:10.1038/s41467-019-09982-5

950 Kent WJ, Sugnet CW, Furey TS, Roskin KM, Pringle TH, Zahler AM, Haussler D. 2002. The
951 Human Genome Browser at UCSC. *Genome Res* **12**:996–1006. doi:10.1101/gr.229102

952 Kim J, Lu C, Srinivasan S, Awe S, Brehm A, Fuller MT. 2017. Blocking promiscuous activation
953 at cryptic promoters directs cell type–specific gene expression. *Science* **356**:717–721.
954 doi:10.1126/science.aal3096

955 Klein DC, Troy K, Tripplehorn SA, Hainer SJ. 2023. The esBAF and ISWI nucleosome
956 remodeling complexes influence occupancy of overlapping dinucleosomes and fragile
957 nucleosomes in murine embryonic stem cells. *BMC Genom* **24**:201. doi:10.1186/s12864-
958 023-09287-4

959 Kloet SL, Baymaz HI, Makowski M, Groenewold V, Jansen PWTC, Berendsen M, Niazi H, Kops
960 GJ, Vermeulen M. 2015. Towards elucidating the stability, dynamics and architecture of
961 the nucleosome remodeling and deacetylase complex by using quantitative interaction
962 proteomics. *Febs J* **282**:1774–1785. doi:10.1111/febs.12972

963 Kong NR, Bassal MA, Tan HK, Kurland JV, Yong KJ, Young JJ, Yang Y, Li F, Lee JD, Liu Y, Wu C-S,
964 Stein A, Luo HR, Silberstein LE, Bulyk ML, Tenen DG, Chai L. 2021. Zinc Finger Protein
965 SALL4 Functions through an AT-Rich Motif to Regulate Gene Expression. *Cell Reports*
966 **34**:108574. doi:10.1016/j.celrep.2020.108574

967 Kubik S, Bruzzone MJ, Jacquet P, Falcone J-L, Rougemont J, Shore D. 2015. Nucleosome
968 Stability Distinguishes Two Different Promoter Types at All Protein-Coding Genes in Yeast.
969 *Mol Cell* **60**:422–434. doi:10.1016/j.molcel.2015.10.002

970 Kubota T, Nishimura K, Kanemaki MT, Donaldson AD. 2013. The Elg1 Replication Factor C-like
971 Complex Functions in PCNA Unloading during DNA Replication. *Mol Cell* **50**:273–280.
972 doi:10.1016/j.molcel.2013.02.012

973 Lai AY, Wade PA. 2011. Cancer biology and NuRD: a multifaceted chromatin remodelling
974 complex. *Nat Rev Cancer* **11**:588–596. doi:10.1038/nrc3091

975 Lambert SA, Jolma A, Campitelli LF, Das PK, Yin Y, Albu M, Chen X, Taipale J, Hughes TR,
976 Weirauch MT. 2018. The Human Transcription Factors. *Cell* **172**:650–665.
977 doi:10.1016/j.cell.2018.01.029

978 Lando D, Ma X, Cao Y, Jartseva A, Stevens TJ, Boucher W, Reynolds N, Montibus B, Hall D,
979 Lackner A, Ragheb R, Leeb M, Hendrich BD, Laue ED. 2024. Enhancer-promoter

980 interactions are reconfigured through the formation of long-range multiway hubs as mouse
981 ES cells exit pluripotency. *Mol Cell* **84**:1406-1421.e8. doi:10.1016/j.molcel.2024.02.015

982 Lauberth SM, Rauchman M. 2006. A Conserved 12-Amino Acid Motif in Sall1 Recruits the
983 Nucleosome Remodeling and Deacetylase Corepressor Complex. *J Biol Chem* **281**:23922–
984 23931. doi:10.1074/jbc.m513461200

985 Lenz J, Brehm A. 2023. Conserved mechanisms of NuRD function in hematopoetic gene
986 expression. *Enzym* 7–32. doi:10.1016/bs.enz.2023.07.006

987 Li H, Durbin R. 2009. Fast and accurate short read alignment with Burrows–Wheeler
988 transform. *Bioinformatics* **25**:1754–1760. doi:10.1093/bioinformatics/btp324

989 Li H, Handsaker B, Wysoker A, Fennell T, Ruan J, Homer N, Marth G, Abecasis G, Durbin R,
990 Subgroup 1000 Genome Project Data Processing. 2009. The Sequence Alignment/Map
991 format and SAMtools. *Bioinformatics* **25**:2078–2079. doi:10.1093/bioinformatics/btp352

992 Liao Y, Smyth GK, Shi W. 2014. featureCounts: an efficient general purpose program for
993 assigning sequence reads to genomic features. *Bioinformatics* **30**:923–930.
994 doi:10.1093/bioinformatics/btt656

995 Love MI, Huber W, Anders S. 2014. Moderated estimation of fold change and dispersion for
996 RNA-seq data with DESeq2. *Genome Biol* **15**:550. doi:10.1186/s13059-014-0550-8

997 Lu F, Lionnet T. 2021. Transcription Factor Dynamics. *Cold Spring Harb Perspect Biol*
998 **13**:a040949. doi:10.1101/cshperspect.a040949

999 Lu J, Jeong H, Kong N, Yang Y, Carroll J, Luo HR, Silberstein LE, YupoMa, Chai L. 2009. Stem
1000 Cell Factor SALL4 Represses the Transcriptions of PTEN and SALL1 through an Epigenetic
1001 Repressor Complex. *Plos One* **4**:e5577. doi:10.1371/journal.pone.0005577

1002 Mahendrawada L, Warfield L, Donczew R, Hahn S. 2025. Low overlap of transcription factor
1003 DNA binding and regulatory targets. *Nature* 1–9. doi:10.1038/s41586-025-08916-0

1004 Martincorena I, Raine KM, Gerstung M, Dawson KJ, Haase K, Loo PV, Davies H, Stratton MR,
1005 Campbell PJ. 2017. Universal Patterns of Selection in Cancer and Somatic Tissues. *Cell*
1006 **171**:1029-1041.e21. doi:10.1016/j.cell.2017.09.042

1007 McDonel P, Costello I, Hendrich B. 2009. Keeping things quiet: Roles of NuRD and Sin3 co-
1008 repressor complexes during mammalian development. *Int J Biochem Cell Biology* **41**:108–
1009 116. doi:10.1016/j.biocel.2008.07.022

1010 Meers MP, Bryson TD, Henikoff JG, Henikoff S. 2019. Improved CUT&RUN chromatin profiling
1011 tools. *eLife* **8**:e46314. doi:10.7554/elife.46314

1012 Miller A, Ralser M, Kloet SL, Loos R, Nishinakamura R, Bertone P, Vermeulen M, Hendrich B.
1013 2016. Sall4 controls differentiation of pluripotent cells independently of the Nucleosome
1014 Remodelling and Deacetylation (NuRD) complex. *Development* **143**:3074–3084.
1015 doi:10.1242/dev.139113

1016 Mindel V, Barkai N. 2025. On the overlap of transcription factor binding and regulatory targets:
1017 functional and regulatory coherence of top-bound targets is masked by weakly bound
1018 ones. *bioRxiv* 2025.10.12.681120. doi:10.1101/2025.10.12.681120

1019 Montibus B, Ragheb R, Diamanti E, Dunn S-J, Reynolds N, Hendrich B. 2023. The Nucleosome
1020 Remodelling and Deacetylation complex coordinates the transcriptional response to
1021 lineage commitment in pluripotent cells. *Biol Open* **13**:bio060101. doi:10.1242/bio.060101

1022 Morris SA, Baek S, Sung M-H, John S, Wiench M, Johnson TA, Schiltz RL, Hager GL. 2014.
1023 Overlapping chromatin-remodeling systems collaborate genome wide at dynamic
1024 chromatin transitions. *Nat Struct Mol Biol* **21**:73–81. doi:10.1038/nsmb.2718

1025 Moshkin YM, Chalkley GE, Kan TW, Reddy BA, Ozgur Z, Ijcken WFJ van, Dekkers DHW,
1026 Demmers JA, Travers AA, Verrijzer CP. 2012. Remodelers Organize Cellular Chromatin by
1027 Counteracting Intrinsic Histone-DNA Sequence Preferences in a Class-Specific Manner.
1028 *Mol Cell Biol* **32**:675–688. doi:10.1128/mcb.06365-11

1029 Mulas C, Kalkan T, Meyenn F von, Leitch HG, Nichols J, Smith A. 2019. Defined conditions for
1030 propagation and manipulation of mouse embryonic stem cells. *Development*
1031 **146**:dev173146. doi:10.1242/dev.173146

1032 Nabet B, Roberts JM, Buckley DL, Paulk J, Dastjerdi S, Yang A, Leggett AL, Erb MA, Lawlor MA,
1033 Souza A, Scott TG, Vittori S, Perry JA, Qi J, Winter GE, Wong K-K, Gray NS, Bradner JE. 2018.
1034 The dTAG system for immediate and target-specific protein degradation. *Nat Chem Biol*
1035 **14**:431–441. doi:10.1038/s41589-018-0021-8

1036 Narlikar GJ, Sundaramoorthy R, Owen-Hughes T. 2013. Mechanisms and Functions of ATP-
1037 Dependent Chromatin-Remodeling Enzymes. *Cell* **154**:490–503.
1038 doi:10.1016/j.cell.2013.07.011

1039 Nishimura K, Fukagawa T, Takisawa H, Kakimoto T, Kanemaki M. 2009. An auxin-based
1040 degron system for the rapid depletion of proteins in nonplant cells. *Nat Methods* **6**:917–
1041 922. doi:10.1038/nmeth.1401

1042 Nishinakamura R, Matsumoto Y, Nakao K, Nakamura K, Sato A, Copeland NG, Gilbert DJ,
1043 Jenkins NA, Scully S, Lacey DL, Katsuki M, Asashima M, Yokota T. 2001. Murine homolog of
1044 SALL1 is essential for ureteric bud invasion in kidney development. *Development*
1045 **128**:3105–3115. doi:10.1242/dev.128.16.3105

1046 Nocente MC, Karamitsos AM, Drouineau E, Soleil M, Albawardi W, Dulary C, Ribierre F,
1047 Picaud H, Alibert O, Acker J, Kervella M, Aude J-C, Gilbert N, Ochsenbein F, Chantalat S,
1048 Gérard M. 2024. cBAF generates subnucleosomes that expand OCT4 binding and function
1049 beyond DNA motifs at enhancers. *Nat Struct Mol Biol* **31**:1756–1768. doi:10.1038/s41594-
1050 024-01344-0

1051 O'Shaughnessy-Kirwan A, Signolet J, Costello I, Gharbi S, Hendrich B. 2015. Constraint of
1052 gene expression by the chromatin remodelling protein CHD4 facilitates lineage
1053 specification. *Development* **142**:2586–2597. doi:10.1242/dev.125450

1054 Ostapcuk V, Mohn F, Carl SH, Basters A, Hess D, Iesmantavicius V, Lampersberger L, Flemr
1055 M, Pandey A, Thomä NH, Betschinger J, Bühler M. 2018. Activity-dependent
1056 neuroprotective protein recruits HP1 and CHD4 to control lineage-specifying genes.
1057 *Nature* **557**:739–743. doi:10.1038/s41586-018-0153-8

1058 Pantier R, Chhatbar K, Quante T, Skourti-Stathaki K, Cholewa-Waclaw J, Alston G, Alexander-
1059 Howden B, Lee HY, Cook AG, Spruijt CG, Vermeulen M, Selfridge J, Bird A. 2021. SALL4
1060 controls cell fate in response to DNA base composition. *Mol Cell* **81**:845-858.e8.
1061 doi:10.1016/j.molcel.2020.11.046

1062 Pavani SRP, Greengard A, Piestun R. 2009. Three-dimensional localization with nanometer
1063 accuracy using a detector-limited double-helix point spread function system. *Appl Phys*
1064 *Lett* **95**:021103. doi:10.1063/1.3158923

1065 Picelli S, Björklund ÅK, Reinius B, Sagasser S, Winberg G, Sandberg R. 2014. Tn5 transposase
1066 and tagmentation procedures for massively scaled sequencing projects. *Genome Res*
1067 **24**:2033–2040. doi:10.1101/gr.177881.114

1068 Pierson TM, Otero MG, Grand K, Choi A, Graham JM, Young JI, Mackay JP. 2019. The NuRD
1069 complex and macrocephaly associated neurodevelopmental disorders. *Am J Medical*
1070 *Genetics Part C Seminars Medical Genetics* **181**:548–556. doi:10.1002/ajmg.c.31752

1071 Pintacuda G, Wei G, Roustan C, Kirmizitas BA, Solcan N, Cerase A, Castello A, Mohammed S,
1072 Moindrot B, Nesterova TB, Brockdorff N. 2017. hnRNPK Recruits PCGF3/5-PRC1 to the Xist
1073 RNA B-Repeat to Establish Polycomb-Mediated Chromosomal Silencing. *Mol Cell* **68**:955-
1074 969.e10. doi:10.1016/j.molcel.2017.11.013

1075 Polo SE, Kaidi A, Baskcomb L, Galanty Y, Jackson SP. 2010. Regulation of DNA-damage
1076 responses and cell-cycle progression by the chromatin remodelling factor CHD4. *Embo J*
1077 **29**:3130–3139. doi:10.1038/emboj.2010.188

1078 Pundhir S, Su J, Tapia M, Hansen AM, Haile JS, Hansen K, Porse BT. 2023. The impact of
1079 SWI/SNF and NuRD inactivation on gene expression is tightly coupled with levels of RNA
1080 polymerase II occupancy at promoters. *Genome Res* **33**:332–345.
1081 doi:10.1101/gr.277089.122

1082 Ragheb R, Gharbi S, Cramard J, Ogundele O, Kloet S, Burgold T, Vermeulen M, Reynolds N,
1083 Hendrich B. 2020. Differential regulation of lineage commitment in human and mouse
1084 primed pluripotent stem cells by the Nucleosome Remodelling and Deacetylation
1085 Complex. *Stem Cell Res* **46**:101867. doi:10.1016/j.scr.2020.101867

1086 Rainer J, Gatto L, Weichenberger CX. 2019. ensembldb: an R package to create and use
1087 Ensembl-based annotation resources. *Bioinformatics* **35**:3151–3153.
1088 doi:10.1093/bioinformatics/btz031

1089 Ramírez F, Dündar F, Diehl S, Grüning BA, Manke T. 2014. deepTools: a flexible platform for
1090 exploring deep-sequencing data. *Nucleic Acids Res* **42**:W187–W191.
1091 doi:10.1093/nar/gku365

1092 Reid XJ, Low JKK, Mackay JP. 2023. A NuRD for all seasons. *Trends Biochem Sci* **48**:11–25.
1093 doi:10.1016/j.tibs.2022.06.002

1094 Reid XJ, Zhong Y, Mackay JP. 2024. How does CHD4 slide nucleosomes? *Biochem Soc Trans*.
1095 doi:10.1042/bst20230070

1096 Reynolds N, Latos P, Hynes-Allen A, Loos R, Leaford D, O'Shaughnessy A, Mosaku O, Signolet
1097 J, Brennecke P, Kalkan T, Costello I, Humphreys P, Mansfield W, Nakagawa K, Strouboulis
1098 J, Behrens A, Bertone P, Hendrich B. 2012. NuRD Suppresses Pluripotency Gene
1099 Expression to Promote Transcriptional Heterogeneity and Lineage Commitment. *Cell Stem*
1100 *Cell* **10**:583–594. doi:10.1016/j.stem.2012.02.020

1101 Ru W, Koga T, Wang X, Guo Q, Gearhart MD, Zhao S, Murphy M, Kawakami H, Corcoran D,
1102 Zhang J, Zhu Z, Yao X, Kawakami Y, Xu C. 2022. Structural studies of SALL family protein
1103 zinc finger cluster domains in complex with DNA reveal preferential binding to an AATA
1104 tetranucleotide motif. *J Biol Chem* **298**:102607. doi:10.1016/j.jbc.2022.102607

1105 Saotome M, Poduval DB, Grimm SA, Nagornyuk A, Gunarathna S, Shimbo T, Wade PA, Takaku
1106 M. 2024. Genomic transcription factor binding site selection is edited by the chromatin
1107 remodeling factor CHD4. *Nucleic Acids Res* **52**:3607–3622. doi:10.1093/nar/gkae025

1108 Schep AN, Buenrostro JD, Denny SK, Schwartz K, Sherlock G, Greenleaf WJ. 2015. Structured
1109 nucleosome fingerprints enable high-resolution mapping of chromatin architecture within
1110 regulatory regions. *Genome Res* **25**:1757–1770. doi:10.1101/gr.192294.115

1111 Schindelin J, Arganda-Carreras I, Frise E, Kaynig V, Longair M, Pietzsch T, Preibisch S, Rueden
1112 C, Saalfeld S, Schmid B, Tinevez J-Y, White DJ, Hartenstein V, Eliceiri K, Tomancak P,
1113 Cardona A. 2012. Fiji: an open-source platform for biological-image analysis. *Nat Methods*
1114 **9**:676–682. doi:10.1038/nmeth.2019

1115 Serizay J, Ahringer J. 2021. Generating fragment density plots in R/Bioconductor with VplotR. *J*
1116 *Open Source Softw* **6**:3009. doi:10.21105/joss.03009

1117 Signolet J, Hendrich B. 2015. The function of chromatin modifiers in lineage commitment and
1118 cell fate specification. *Febs J* **282**:1692–1702. doi:10.1111/febs.13132

1119 Smeenk G, Wiegant WW, Vrolijk H, Solari AP, Pastink A, Attikum H van. 2010. The NuRD
1120 chromatin–remodeling complex regulates signaling and repair of DNA damage. *J Cell*
1121 *Biology* **190**:741–749. doi:10.1083/jcb.201001048

1122 Sreenivasan K, Rodríguez-delaRosa A, Kim J, Mesquita D, Segalés J, Arco PG, Espejo I, Ianni A,
1123 Croce LD, Relaix F, Redondo JM, Braun T, Serrano AL, Perdiguero E, Muñoz-Cánoves P.
1124 2021. CHD4 ensures stem cell lineage fidelity during skeletal muscle regeneration. *Stem*
1125 *Cell Rep* **16**:2089–2098. doi:10.1016/j.stemcr.2021.07.022

1126 Srivastava D, Mahony S. 2020. Sequence and chromatin determinants of transcription factor
1127 binding and the establishment of cell type-specific binding patterns. *Biochim Biophys Acta*
1128 *(BBA) - Gene Regul Mech* **1863**:194443. doi:10.1016/j.bbagrm.2019.194443

1129 Stevens TJ, Lando D, Basu S, Atkinson LP, Cao Y, Lee SF, Leeb M, Wohlfahrt KJ, Boucher W,
1130 O'Shaughnessy-Kirwan A, Cramard J, Faure AJ, Ralser M, Blanco E, Morey L, Sansó M,
1131 Palayret MGS, Lehner B, Croce LD, Wutz A, Hendrich B, Klenerman D, Laue ED. 2017. 3D
1132 structures of individual mammalian genomes studied by single-cell Hi-C. *Nature* **544**:59–
1133 64. doi:10.1038/nature21429

1134 Tokunaga M, Imamoto N, Sakata-Sogawa K. 2008. Highly inclined thin illumination enables
1135 clear single-molecule imaging in cells. *Nat Methods* **5**:159–161. doi:10.1038/nmeth1171

1136 Wade PA, Jones PL, Vermaak D, Wolffe AP. 1998. A multiple subunit Mi-2 histone deacetylase
1137 from Xenopus laevis cofractionates with an associated Snf2 superfamily ATPase. *Curr Biol*
1138 **8**:843–848. doi:10.1016/s0960-9822(98)70328-8

1139 Watson JA, Pantier R, Jayachandran U, Chhatbar K, Alexander-Howden B, Kruusvee V,
1140 Prendecki M, Bird A, Cook AG. 2023. Structure of SALL4 zinc finger domain reveals link
1141 between AT-rich DNA binding and Okihiro syndrome. *Life Sci Alliance* **6**:e202201588.
1142 doi:10.26508/lsa.202201588

1143 Wilczewski CM, Hepperla AJ, Shimbo T, Wasson L, Robbe ZL, Davis IJ, Wade PA, Conlon FL.
1144 2018. CHD4 and the NuRD complex directly control cardiac sarcomere formation. *Proc*
1145 *National Acad Sci* **115**:201722219. doi:10.1073/pnas.1722219115

1146 Williams CJ, Naito T, Arco PG, Seavitt JR, Cashman SM, Souza BD, Qi X, Keables P, Andrian
1147 UHV, Georgopoulos K. 2004. The Chromatin Remodeler Mi-2β Is Required for CD4
1148 Expression and T Cell Development. *Immunity* **20**:719–733.
1149 doi:10.1016/j.immuni.2004.05.005

1150 Wilson BG, Roberts CWM. 2011. SWI/SNF nucleosome remodellers and cancer. *Nat Rev*
1151 *Cancer* **11**:481–492. doi:10.1038/nrc3068

1152 Wit E de, Nora EP. 2023. New insights into genome folding by loop extrusion from inducible
1153 degron technologies. *Nat Rev Genet* **24**:73–85. doi:10.1038/s41576-022-00530-4

1154 Workman JL, Buchman AR. 1993. Multiple functions of nucleosomes and regulatory factors in
1155 transcription. *Trends Biochem Sci* **18**:90–95. doi:10.1016/0968-0004(93)90160-o

1156 Wu H, Muñoz EN, Hsieh LJ, Chio US, Gourdet MA, Narlikar GJ, Cheng Y. 2023. Reorientation of
1157 INO80 on hexasomes reveals basis for mechanistic versatility. *Science* **381**:319–324.
1158 doi:10.1126/science.adf4197

1159 Xi Y, Yao J, Chen R, Li W, He X. 2011. Nucleosome fragility reveals novel functional states of
1160 chromatin and poises genes for activation. *Genome Res* **21**:718–724.
1161 doi:10.1101/gr.117101.110

1162 Xue Y, Wong J, Moreno GT, Young MK, Côté J, Wang W. 1998. NURD, a Novel Complex with
1163 Both ATP-Dependent Chromatin-Remodeling and Histone Deacetylase Activities. *Mol Cell*
1164 **2**:851–861. doi:10.1016/s1097-2765(00)80299-3

1165 Yoshida T, Hu Y, Zhang Z, Emmanuel AO, Galani K, Muhire B, Snippert HJ, Williams CJ,
1166 Tolstorukov MY, Gounari F, Georgopoulos K. 2019. Chromatin restriction by the

1167 nucleosome remodeler Mi-2β and functional interplay with lineage-specific transcription
1168 regulators control B-cell differentiation. *Genes Dev* **33**:763–781.
1169 doi:10.1101/gad.321901.118

1170 Yu G, Wang L-G, Han Y, He Q-Y. 2012. clusterProfiler: an R Package for Comparing Biological
1171 Themes Among Gene Clusters. *OMICS: A J Integr Biol* **16**:284–287.
1172 doi:10.1089/omi.2011.0118

1173 Zhang M, Jungblut A, Kunert F, Hauptmann L, Hoffmann T, Kolesnikova O, Metzner F, Moldt M,
1174 Weis F, DiMaio F, Hopfner K-P, Eustermann S. 2023. Hexasome-INO80 complex reveals
1175 structural basis of noncanonical nucleosome remodeling. *Science* **381**:313–319.
1176 doi:10.1126/science.adf6287

1177 Zhang W, Aubert A, Segura JMG de, Karuppasamy M, Basu S, Murthy AS, Diamante A, Drury
1178 TA, Balmer J, Cramard J, Watson AA, Lando D, Lee SF, Palayret M, Kloet SL, Smits AH,
1179 Deery MJ, Vermeulen M, Hendrich B, Klenerman D, Schaffitzel C, Berger I, Laue ED. 2016.
1180 The Nucleosome Remodeling and Deacetylase Complex NuRD Is Built from Preformed
1181 Catalytically Active Sub-modules. *J Mol Biol* **428**:2931–2942.
1182 doi:10.1016/j.jmb.2016.04.025

1183 Zhang Y, LeRoy G, Seelig H-P, Lane WS, Reinberg D. 1998. The Dermatomyositis-Specific
1184 Autoantigen Mi2 Is a Component of a Complex Containing Histone Deacetylase and
1185 Nucleosome Remodeling Activities. *Cell* **95**:279–289. doi:10.1016/s0092-8674(00)81758-4

1186 Zhang Y, Liu T, Meyer CA, Eeckhoute J, Johnson DS, Bernstein BE, Nusbaum C, Myers RM,
1187 Brown M, Li W, Liu XS. 2008. Model-based analysis of ChIP-Seq (MACS). *Genome Biol*
1188 **9**:R137. doi:10.1186/gb-2008-9-9-r137

1189 Zhong Y, Paudel BP, Ryan DP, Low JKK, Franck C, Patel K, Bedward MJ, Torrado M, Payne RJ,
1190 Oijen AM van, Mackay JP. 2020. CHD4 slides nucleosomes by decoupling entry- and exit-
1191 side DNA translocation. *Nat Commun* **11**:1519. doi:10.1038/s41467-020-15183-2

1192 Zhu F, Farnung L, Kaasinen E, Sahu B, Yin Y, Wei B, Dodonova SO, Nitta KR, Morgunova E,
1193 Taipale M, Cramer P, Taipale J. 2018. The interaction landscape between transcription
1194 factors and the nucleosome. *Nature* **562**:76–81. doi:10.1038/s41586-018-0549-5

Supplemental Figure 1

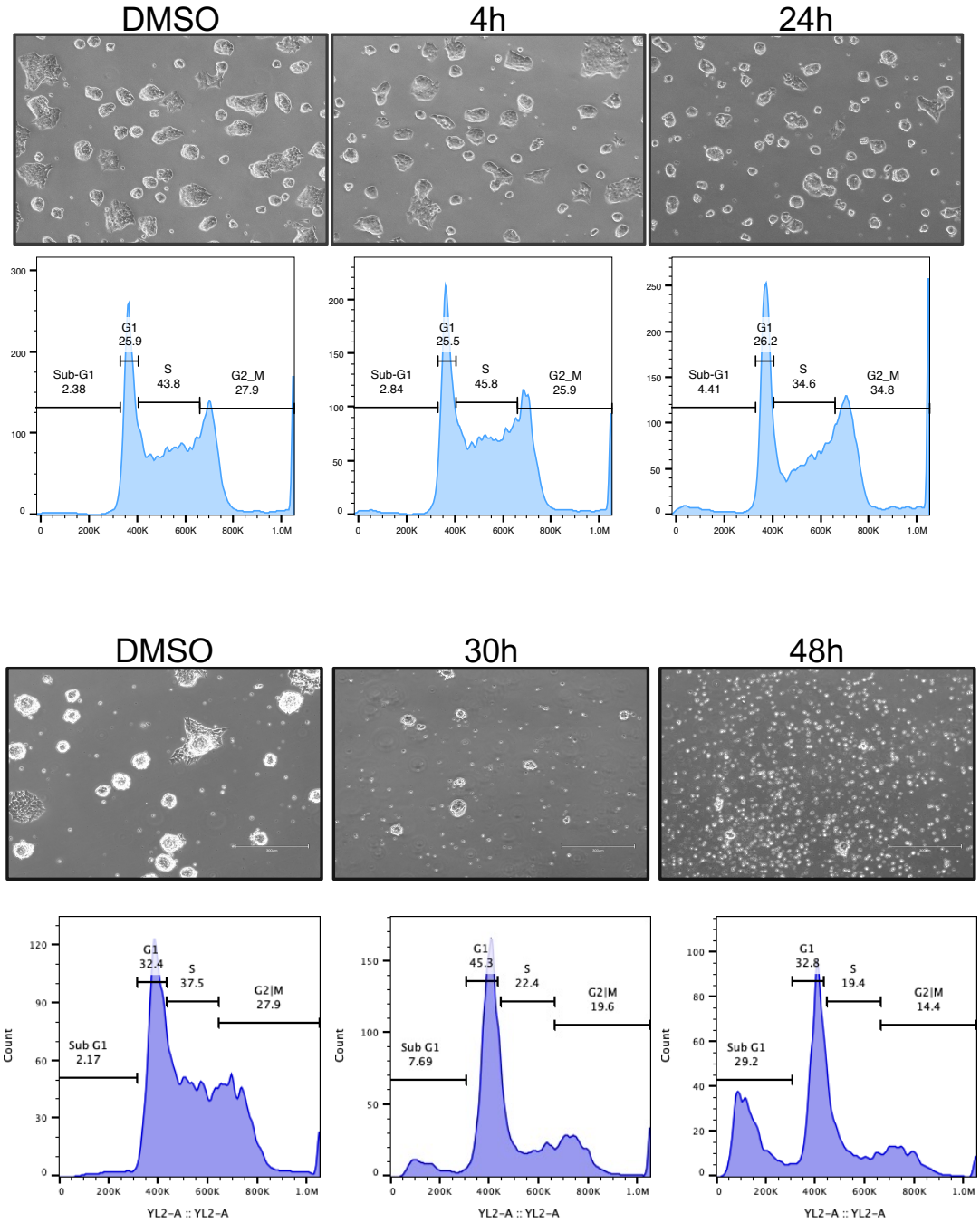

Supplemental Figure 1. Cell cycle arrest and cell death following CHD4 depletion. Phase contrast images and example flow cytometry plots of CHD4-mAID ES cells in 2iL conditions after indicated times of Auxin addition. Cell cycle stage and relative percentage of cells are indicated on the flow cytometry plots.

Supplemental Figure 2

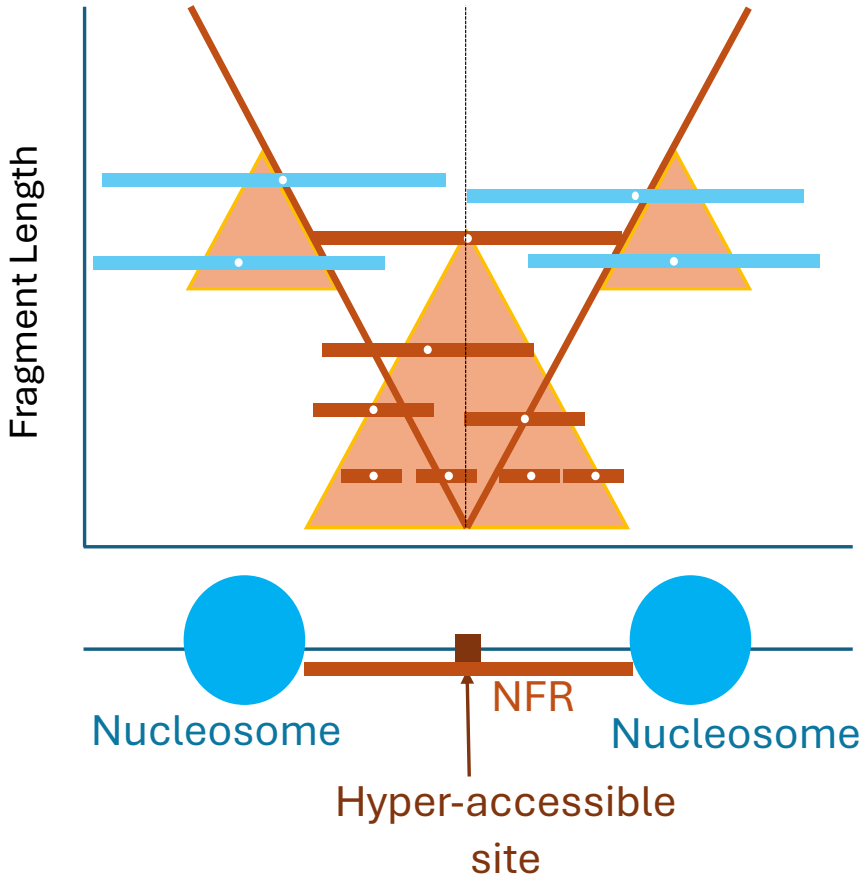

Supplemental Figure 2. **Schematic diagram of Vplots.** Adapted from (Henikoff et al., 2011) . The Vplot is derived by plotting the midpoint of all recovered fragments (horizontal lines) onto the graph, with midpoint position (white circle) on the x-axis and fragment length on the y-axis. Red lines correspond to reads obtained from fragments with both ends (i.e. Tn5 integration sites) in the NFR, while blue lines represent reads spanning a nucleosome. The vertical dotted line indicates the position of the central hyperaccessible site. The inferred chromatin structure of the locus is shown below.